Ultrasonics Sonochemistry 73 (2021) 105490

Contents lists available at ScienceDirect

Ultrasonics Sonochemistry

journal homepage: www.elsevier.com/locate/ultson

Ultrasound-assisted sequentially precipitated nickel-silica catalysts and its application in the partial hydrogenation of edible oil

Mitchell S.W. Lim [a], Thomas Chung-Kuang Yang [b], T. Joyce Tiong [a], Guan-Ting Pan [b], Siewhui Chong [a], Yeow Hong Yap [c,*]

[a] Department of Chemical and Environmental Engineering, University of Nottingham Malaysia, Jalan Broga, 43500 Semenyih, Selangor, Malaysia
[b] Department of Chemical Engineering and Biotechnology, National Taipei University of Technology, Taipei, Taiwan
[c] Department of Chemical Engineering, Lee Kong Chian Faculty of Engineering and Science, Universiti Tunku Abdul Rahman, Bandar Sg. Long, 43000 Kajang, Selangor, Malaysia

ARTICLE INFO

Keywords:
Ultrasonic irradiation
Hydrogenation
Nickel-silica
Catalyst synthesis
Sequential precipitation
Catalyst ageing

ABSTRACT

Sequentially precipitated Mg-promoted nickel-silica catalysts with ageing performed under various ultrasonic intensities were employed to study the catalyst performance in the partial hydrogenation of sunflower oil. Results from various characterisation studies showed that increasing ultrasonic intensity caused a higher degree of hydroxycarbonate erosion and suppressed the formation of Ni silicates and silica support, which improved Ni dispersion, BET surface area and catalyst reducibility. Growth of silica clusters on the catalyst aggregates were observed in the absence of ultrasonication, which explained the higher silica and nickel silicate content on the outer surface of the catalyst particle. Application of ultrasound also altered the electron density of the Ni species, which led to higher activity and enhanced product selectivity for sonicated catalysts. The catalyst synthesised with ultrasonic intensity of 20.78 Wcm^{-2} achieved 22.6% increase in hydrogenation activity, along with 28.5% decrease in *trans*-C18:1 yield at IV = 70, thus supporting the feasibility of such technique.

1. Introduction

In the industry, the catalytic hydrogenation of edible oils is typically carried out in a slurry reactor through a semi-batch process, with H_2 gas injected at an elevated temperature and pressure [1]. One of the most imperative aspects of the process is the usage of a catalyst to catalyse the reaction. Although Ni-based catalysts are vastly applied in industrial processes due to their superior performance and cost effectiveness, constant improvement is vital to further enhance the activity and selectivity of the catalysts. Various preparation parameters have been studied e.g. support type, active metal content, reduction temperature, presence of doping agents, synthesis methods, etc. [2–5]. To illustrate, some of these properties such as the pore volume, pore length, particle size, total surface area and Ni crystallite size play a crucial role in determining the activity and selectivity of the catalysts [6,7]. In particular, a high pore volume, shorter pore length, smaller particle size, larger total surface area and smaller Ni crystallite size would potentially benefit the catalytic activity of the catalyst [8,9].

The co-precipitation of a Ni salt and a silica source using an alkali source such as sodium carbonate is one of the common and conventional techniques to synthesise Ni catalyst precursors i.e. silica-supported Ni carbonate. The aforementioned substance yields supported Ni catalysts upon reduction [10]. Nitta and colleagues have concluded that compounds of Ni, particularly hydroxide or carbonate compounds of Ni, tend to form strong interactions with the silica carrier or support. Consequently, this results in the generation of Ni hydrosilicate phases, particularly nickel phyllosilicates, on the external layers of the support phase, which function as anchoring sites for Ni particles, leading to their stabilisation and dispersion [11]. This phenomenon is also supported by various other work concerning the synthesis of silica-supported Ni catalysts [2,12–14]. The presence of these metal-support interactions (MSI) could potentially influence the properties and performance of heterogeneous supported catalysts in terms of their active metallic area and dispersion, reducibility and stability or resistance to thermal sintering, and subsequently the activity and selectivity [3,15,16]. As described in some studies, many factors could influence these properties, including the catalyst synthesis technique. For instance, it was reported that the ageing step is of substantial significance in dictating fundamental

* Corresponding author.
E-mail address: yapyh@utar.edu.my (Y.H. Yap).

https://doi.org/10.1016/j.ultsonch.2021.105490
Received 20 December 2020; Received in revised form 26 January 2021; Accepted 2 February 2021
Available online 10 February 2021

catalyst properties, which controls the degree of formation of less reducible silicates, therefore affecting final metallic dispersion and surface area properties [17,18]. In particular, ageing time and ageing temperature were reported to play an important role in tuning nickel silicate formation, ultimately influencing catalyst activity and applicability [18].

Among numerous catalyst synthesis techniques, ultrasonic technology has emerged over the years as an innovative method to effectively modify the properties and performance of heterogeneous catalysts [19–21]. The incorporation of ultrasonic irradiation into catalyst synthesis could result in various changes in particle morphology, surface composition, metal dispersion, structural or geometric properties, electronic configurations and catalyst reactivity [19,22,23]. In some cases, the use of ultrasound is able to activate less reactive, but also less costly, catalytic metals [24]. To illustrate, in liquids irradiated by ultrasound, the phenomenon known as acoustic cavitation induces the formation and subsequent implosion of numerous short-lived micro-bubbles with extremely high temperatures and pressures [25]. These transient, localised hot-spots facilitate various physical and chemical reactions during catalyst synthesis, which brings about the enhancement and promotion of nucleation rates and dispersion of active metals on the support surface [26]. Nevertheless, it is also imperative to understand the underlying mechanisms involved in driving the positive effects demonstrated by ultrasonic irradiation in catalyst synthesis, which is an aspect that many literature sources lack. For instance, in various catalysts synthesised for photocatalytic, catalytic cracking and gas reforming applications, authors have reported the increase in reducibility, metal dispersion, particle uniformity, BET surface area etc. [19,27–34] with the use of ultrasound during synthesis but detailed explanations for the reason behind the improvement were generally lacking. It is also important to note that performing routine calibration experiments is imperative to accurately reflect the actual acoustic power dissipated by the ultrasonic source, which could allow effective replications as well as comparisons between different bodies of work. This in fact is a critical aspect that a large majority of literature sources lack, whereby only the electric powers specified by the ultrasonic generators (as provided by manufacturers) are detailed [19,27–29,32,34,35].

Prompted by this knowledge gap, this present work aims to study the phenomenon and mechanisms that take place during the synthesis of sequentially precipitated catalysts with ultrasound employed during the ageing step. Specifically, nickel-silica hydrogenation catalysts were synthesised via sequential precipitation, with ultrasonic irradiation applied at varying ultrasonic intensities during the ageing step, whereby the actual acoustic powers supplied were determined. The catalysts were evaluated based on several characterisation tests, in which the variation in catalyst phase compositions due to sonication was analysed and the ultrasonic irradiation synthesis mechanism was outlined. To further appraise the performance of the synthesised catalysts, the partial hydrogenation of sunflower oil was carried out to ascertain the activity and selectivity of the catalysts.

2. Experimental

Chemicals used in this work were of analytical grade, obtained from R&M Chemicals Malaysia, utilised without supplemental purification. The ultrasonic system employed in this study was fitted with a 20 kHz probe. The diameter of the probe tip was approximately 1 cm (Sonics and Materials, VCX 750, 750 W). O'life Sunflower oil (Sime Darby Food and Marketing Sdn. Bhd., Malaysia) was employed as the feed for the hydrogenation reaction. The iodine value (IV) of the feed was 124, with its composition listed in Table 1.

2.1. Calorimetry

To obtain the calorimetry data for the ultrasonic system used, a beaker of 200 ml deionised water was subjected to irradiation with ultrasonic amplitudes of 20, 30 and 40%, total duration being 30 min. The temperature of the system was not regulated. The power output of the ultrasonic system, Q, was obtained using the following equation:

$$Q = \frac{mC_p\Delta T}{\Delta t} \quad (1)$$

where m is the total mass of water, C_p specific heat capacity of water (4.18 kJ kg^{-1} $°C^{-1}$), $\Delta T/\Delta t$ ($°C\ s^{-1}$) is the temperature gradient. Temperature readings were repeated at 30 s intervals and taken at three varied positions in the beaker, noting the mean value.

To ascertain the heat dissipated by the system, water at an equal volume to the ultrasonic set was heated using a portable electric heater of 1000 W, while being stirred. Similarly, the process took 30 min and readings were repeated at 30 s intervals and taken at three varied positions in the beaker, noting the mean value. The power output due to heating, Q_H, can be acquired using Eq. (2). Hence, the heat dissipated, Q_{HL}, can be obtained using the following equation:

$$Q_{HL} = Q_H - Q \quad (2)$$

Subsequently, the acoustic energy intensity provided by the probe, I_{US}, is calculated via the following equation:

$$I_{US} = \frac{Q + Q_{HL}}{A} \quad (3)$$

where

$Q + Q_{HL}$ is the output power, P_{out}, and A is the cross-sectional area of the surface producing ultrasonic waves, determined as 0.8 cm^2 for the ultrasonic probe.

In addition, the ultrasonic density provided by the probe to the liquid body, ρ_{US}, is calculated via the following equation:

$$\rho_{US} = \frac{Q + Q_{HL}}{V} \quad (4)$$

where

V is the volume of water (cm^3) in the beaker used for the calorimetry test.

Table 1
Fatty acid constituents of the sunflower oil employed in this study.

Compounds	Percentage (%)
Palmitic acid (C16:0)	6
Stearic acid (C18:0)	3.3
Oleic acid (*cis*-C18:1)	42
Elaidic acid (*trans*-C18:1)	0
Linoleic acid (C18:2)	48.4

2.2. Catalyst synthesis

Solutions of nickel sulphate hexahydrate ($Ni(SO_4)_2{\cdot}6H_2O$) and magnesium sulphate heptahydrate ($Mg(SO_4)_2{\cdot}7H_2O$) were mixed with a molar ratio of 3:1 and subsequently heated to 50 °C. Then, 10 wt% sodium carbonate (Na_2CO_3) was dosed until the pH of the precipitated suspension was 8.8, in a duration of 10 min. The suspension was then heated to 90 °C, followed by the addition of 2 wt% sodium metasilicate pentahydrate ($Na_2SiO_3{\cdot}5H_2O$) solution, in a duration of 10 min. The suspension was then allowed to age for 30 min at 90 °C. Throughout the whole synthesis process, the suspension was stirred constantly. After terminating the synthesis procedure, the resulting mixture was filtered and thoroughly rinsed using deionised water three times. Next, the filtered precipitate was dried at 100 °C for 5 h in an oven. Lastly, the dried precipitate was calcined in a chamber furnace at 400 °C for 4 h. The unsonicated sample is labelled as A.

For catalysts subjected to ultrasonic irradiation, the dosing of 2 wt% $Na_2SiO_3{\cdot}5H_2O$ solution was delivered under the influence of a sonicator, in the same duration of 10 min as the unsonicated sample for

consistency. The probe was immersed at a depth of 2 cm, pulsed at 2 s on/off, under temperature-controlled conditions. Three sonicated catalysts were synthesised with ultrasonic amplitudes of 20, 30 and 40%, corresponding to ultrasonic intensities of 7.07, 20.78 and 27.72 W cm^{-2}, labelled as B, C and D, respectively. The aforementioned ultrasonic amplitudes were chosen considering their interesting impacts on catalyst synthesis in a previous work [36].

2.3. Catalyst characterisation

2.3.1. Field emission scanning electron microscopy (FE-SEM)

The morphology of the samples was characterised with a field emission scanning electron microscopy (FE-SEM, Fei Quanta 400F). SEM scans were obtained with a Fei Quanta 400F microscope. The beam current was 1 μA and the accelerating voltage was 20 kV.

2.3.2. Energy dispersive X-ray (EDX) analysis

A field emission scanning electron microscope (FE-SEM) fitted with an Oxford Instruments X-MAX energy dispersive X-ray (EDX) analyser was used to obtain the elemental information of the catalysts. The accelerating voltage was 20.0 kV with an acquisition live-time of 45 s.

2.3.3. X-ray powder diffraction (XRD)

The PANalytical X'Pert-PRO diffractometer was used to obtain diffractograms for the catalysts. Cu-Kα X-ray radiation used was of the wavelength 1.54060 Å. The beam current was 40 mA. While the voltage was 45 kV. Crystallite sizes of the samples was ascertained via the Debye-Scherrer's formula.

2.3.4. Brunauer-Emmett-Teller (BET) analysis

The specific surface areas (S_{BET}) and the porosities of the catalysts were acquired with the Micromeritics 3Flex Surface and Catalyst Characterisation Analyser by using the Brunauer-Emmett-Teller method. Adsorption and desorption runs were executed at −195.681 °C (77 K) using N_2 gas. The catalysts were degassed at 150 °C for 4 h before the adsorption experiments.

2.3.5. Temperature programmed reduction (H_2-TPR)

Temperature programmed reduction was carried out with the Micromeritics AutoChem II 2920 chemisorption analyser fitted with a thermal conductivity detector. Approximately 30 mg of the sample were carefully inserted into the quartz U-tube reactor and then placed in the tubular furnace. Catalysts were subjected to pre-treatment under Ar flow at 20 cm^3/min, with the temperature raised from ambient to 100 °C and held for 60 min to remove physisorbed and/or weakly bound species. Subsequently, the catalysts were analysed in 9.47% of H_2/Ar at a flow rate of 25 cm^3/min from ambient to 900 °C at a heating rate of 10 °C/min. The vapour produced is removed via a cold trap filled with chilled coolant. H_2 adsorbed by the catalysts was detected by the thermal conductivity detector and ascertained via the peak area of the H_2-TPR profile. The TPR curves were further processed and deconvoluted using the OriginPro software via Gaussian multi-curve fitting.

2.3.6. Hydrogen pulse chemisorption

Pulse chemisorption analysis was conducted using the Micromeritics AutoChem II 2920 chemisorption analyser. Samples were first degassed in an inert argon gas flow for 60 min at 100 °C. Then, the catalysts were reduced at 500 °C in H_2 for 2 h and degassed once more for 30 min prior to the chemisorption analysis. For the analysis, hydrogen gas was pulsed every 6 min until no further uptake was detected. The Ni metal dispersion (%) is calculated with the following equation:

$$\%Dispersion = \left(\frac{\frac{V_m}{V_{mol}}}{\frac{M_{\%}}{W_a}}\right)(F_s) \quad (5)$$

where

V_m is the volume of hydrogen gas chemisorbed (cm^3/g STP); V_{mol} is the molar volume of the adsorptive (cm^3/mole STP); $M_{\%}$ is the percentage of Ni metal by weight as grams of Ni per gram of sample; W_a is the atomic weight of Ni (g/mole); F_s is the stoichiometry factor, taken as 2 for hydrogen on Ni.

The active metal surface area (m^2/g) is calculated with the following equation:

$$Metal\ surface\ area = F_s n_a N_A A_g \quad (6)$$

where

F_s is the stoichiometry factor, taken as 2 for hydrogen on Ni; n_a is the number of moles of gas adsorbed (cm^3/g STP); N_A is Avogadro's constant; A_g is the cross-sectional area of the active adsorptive atom (nm^2) (with the assumption that a single Ni atom occupies 0.0649 nm^2) [37].

The average metal particle size (nm) is calculated with the following equation [38]:

$$Average\ particle\ size = \frac{6}{(A_{Sm})(\%Dispersion)(\rho)}\ X\ 100 \quad (7)$$

where

A_{Sm} is the active metal surface area (m^2/g); ρ is the density of the metal (g/cm^3).

2.3.7. X-ray photoelectron spectroscopy (XPS)

X-ray photoelectron spectroscopy (XPS) was conducted with the JEOL JPS-9030 photoelectron spectrometer. Al Kα (1486.6 eV) was used as the excitation source to probe the sample surface information at a depth of 1 – 12 nm. The pressure in the analysis chamber during experiments was less than 5×10^{-10} Torr. A hemispherical electron-energy analyser working at a pass energy of 30 eV was used to collect core-level spectra. The samples were dispersed in ethanol and placed on silicon wafers, which were mounted on a sample holder and directly transferred into the analysis chamber. Step size was adjusted to 0.1 eV, dwell time was set at 100 ms and the high-resolution spectra were recorded with 10 scans. Charge effects were corrected by using the C 1 s peak at 285 eV. A Shirley background was applied to subtract the inelastic background of core-level peaks. The model peak to describe XPS core-level lines for curve fitting was a product of Gaussian functions. The XPS spectra were processed and deconvoluted using the OriginPro software.

2.3.8. Atomic absorption spectroscopy (AAS)

Atomic absorption spectroscopy (AAS) was conducted with a Perkin Elmer AAnalyst400 AA spectrometer to obtain the concentration of leached nickel from the hydrogenated oil samples. Sample readings were taken three times to obtain an average value.

2.4. Catalyst reduction

Prior to carrying out the hydrogenation reaction tests, the catalyst samples involved were reduced in pure hydrogen gas for activation. The samples were reduced in a tubular furnace. Before reduction, the samples were heated to 500 °C with a heating rate of 10 °C/min in N_2. Upon reaching 500 °C, the samples were subjected to a flow of hydrogen gas and held for 2 h. Lastly, fully hydrogenated palm stearin (iodine value <0.5) was used to coat the catalysts to prevent oxidation, thus forming fat-coated catalyst granules of 22 wt% Ni.

2.5. Catalyst performance evaluation via partial hydrogenation

Partial hydrogenation was carried out in a 1.5 L pressurised batch reactor (Buchiglasuster Eco-Clave). The temperature of the reactor was regulated by a high precision temperature regulatory system (Huber

Unistat Tango Nuevo), with the use of a silicone oil jacket around the circular reactor and a temperature probe inside the reactor. Briefly, 750 ml of sunflower oil was added into the reactor with the aid of a vacuum pump and heated to a set-point temperature of 180 °C. Prior to dosing the catalyst, the reactor was vacuumed to remove any air or moisture that will poison and deactivate the catalyst. Subsequently, a catalyst dosage of 2 g/L was used and hydrogen gas of 5 barg was charged into the reactor to initiate the reaction, while the slurry was vigorously stirrer at 1500 rpm. Oil samples (4–5 ml) were taken from the bottom of the reactor for each time interval. The reaction was carried out for 90 min. Obtained samples were labelled and filtered using filter papers to remove the catalyst particles.

2.5.1. Determination of iodine value (IV)

The iodine value measures the degree of unsaturation of fats and oils, which represents the mass (g) of iodine consumed per 100 g of oil. Products collected from the reactor were subjected to iodine value tests, in accordance with the American Oil Chemist's Society (AOCS) Official Method Tg 1a-64, performed 3 times to obtain average values. The resulting iodine value was calculated with the following formula:

$$Iodine\ value = \frac{(B - S) \times N \times 12.691}{mass\ of\ sample,\ g} \quad (8)$$

where

B is the volume of titrant of blank set, mL; S is the volume of titrant of sample set, mL; N is the normality of the sodium thiosulphate solution.

2.5.2. Gas chromatography (GC) analysis

Gas chromatography was carried out in order to ascertain their respective fatty acid compositions of the reaction products. A PerkinElmer Clarus 500 gas chromatograph fitted with a PerkinElmer COL-ELITE-2560 capillary column (100 m × 0.25 mm ID × 0.20 μm df). Helium was utilised as the carrier gas at 1.3 ml/min. Prior to the tests, esterification of the hydrogenation products was carried out to convert them into fatty acid methyl esters (FAME). The oven, injector and flame ionisation detector (FID) temperatures were 175, 210 and 250 °C, respectively. The injection volume was 1 μL and the split ratio was 100:1. The relative areas of the fatty acid peaks obtained from the chromatogram were used to determine the product distribution of the oil samples.

3. Results and discussion

3.1. Ultrasonic probe calorimetry

The ultrasonic system was assessed for its calorimetry and results are presented in Table 2. The heat loss, Q_{HL}, calculated was 0.8 W.

3.2. Characterisation of synthesised catalysts

The morphology of the catalysts was interpreted via the SEM scans in Fig. 1. While the non-sonicated catalyst exhibited rough surfaces with the presence of conglomerates, the morphology of the sonicated catalysts all appeared to be smooth and uniform, which confirmed the capability of ultrasound to reduce the extent of particle aggregation [39]. As demonstrated later, the combination of ultrasound irradiation and co-precipitation generated a synergistic effect whereby a uniform environment was provided for the nucleation and growth of metal particles, while concurrently averting small particles from agglomerating [40], thus preventing the formation of aggregates such as those in the non-sonicated catalyst. In particular, the increased ultrasonic intensity instigated more violent micro-bubble implosions, hence inducing stronger shock waves and micro-jets with velocities of approximately 400 km/h. Consequently, vigorous inter-particle collisions and surface pitting could occur, simultaneously suppressing the aggregation of catalyst particles, thus producing particles with increased dispersion [41]. This observed phenomenon resonated with the work of other researchers, in which a lower degree of particle agglomeration was noticed with the use of ultrasound during synthesis [40,42].

Table 2
Ultrasonic power output, intensity and density acquired for the 20 kHz ultrasonic probe.

Ultrasonic amplitude (%)	Rate of increase in temperature, $\frac{\Delta T}{\Delta t}$ (K s^{-1})	Power output, Q (W)	Total power, $Q + Q_{HL}$ (W)	Ultrasonic intensity, I_{US} (W cm^{-2})	Acoustic energy density, ρ_{US} (W cm^{-3})
20	0.005778	4.853	5.653	7.07	0.0283
30	0.01883	15.82	16.62	20.78	0.0831
40	0.02544	21.37	22.17	27.72	0.111

From the EDX and XPS analyses of the synthesised catalysts in Table 3, it is apparent that they were constituted of the required elements to form the catalysts, which indicates the efficacy of the synthesis procedure. As the typical approximated penetration depth of an EDX electron beam is 0.4 μm [43], the measured atomic percentage was considered to represent the bulk atomic percentage of the catalysts. On the other hand, characterisation by XPS detects the elemental composition of the samples at the surface layer, which corresponds to a penetration depth of approximately 1 – 12 nm, hence demonstrative of the superficial composition of the catalysts [43]. As the catalysts investigated were all synthesised according to the same starting materials, it will be useful to draw comparisons based on their bulk and surface atomic distributions to ascertain the changes due to the difference in synthesis conditions. As shown in Table 3, there were decreasing trends for the Mg/Ni and Si/Ni atomic ratios with the increase in ultrasound intensity during the ageing process from data obtained from both EDX and XPS analyses. It is worth noting that while the difference was small for the Mg/Ni ratios between the EDX and XPS methods, there was a substantial gap in the Si/Ni ratios between the two aforementioned methods. We believe the observed change in Mg/Ni and Si/Ni atomic ratios was mainly due to the effect of ultrasonic intensity (or lack thereof) on the sequentially co-precipitated Ni-Mg hydroxycarbonates and siliceous materials during the ageing process.

A conceptualisation demonstrating the action of ultrasound during the ageing process is presented in Fig. 2. It is herein noted that, for the sake of accuracy, prefixes such as hydro- or hydroxy- are used to represent the actual phases of the precursors present during synthesis. After the synthesis process, the aforementioned phases were subjected to dehydration and calcination and subsequently transformed into their respective oxides or silicates, which were then used for characterisations mentioned in this present work. In conventional synthesis of sequentially precipitated catalysts without the presence of ultrasound, the formation of Ni silicate proceeded as the silica precursor was added during the ageing process, which occurs under an alkaline condition at elevated temperatures. Prior to the ageing process, co-precipitates of Ni-Mg hydroxycarbonates were present in the suspension. As the ageing process was initiated, silicate ions (in the form of Na_2SiO_3) were dosed into the ageing solution, which then: (i) attached epitaxially to the co-precipitates [44], forming nickel hydrosilicates, in which Ni-Mg hydroxycarbonates would then be anchored; (ii) attached to existing hydrosilicates and underwent polymerisation to form silica clusters [45]. This attachment of silicate ions is illustrated by Step 1 in Fig. 2. In the presence of ultrasonic irradiation, the Ni-Mg hydroxycarbonate co-precipitates can experience erosion, causing the shrinkage of the size of the co-precipitates, which will eventually lead to higher Ni dispersion as we will see in Table 4. The increase in ultrasound intensity also led to lower Mg/Ni ratios, beginning with sample A at 0.329 (theoretical ratio = 0.333 with Ni:Mg = 3:1) and down to 0.268 for sample D. During the formation of Ni-Mg hydroxycarbonate nanoparticles, Mg has the tendency to migrate to surficial layers due to its lower surface energy

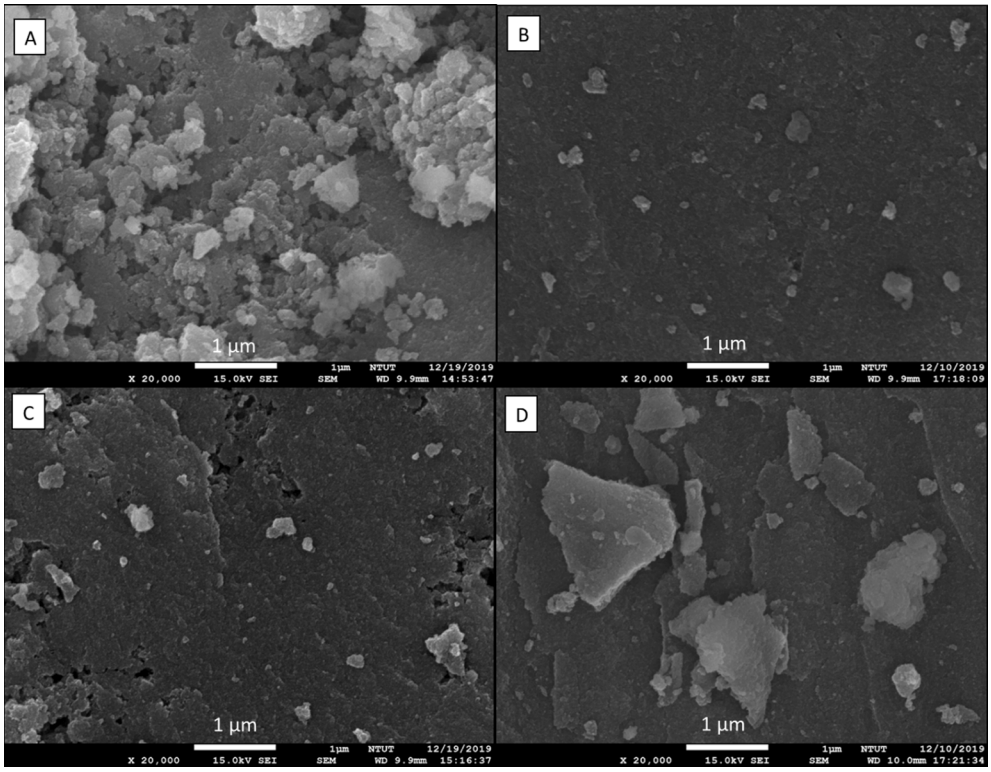

Fig. 1. SEM scans for catalysts A, B, C and D. Note: Micrographs are of 20,000x magnification and 1 μm scale.

Table 3
Elemental composition of the calcined catalysts and molar ratios obtained from EDX and XPS.

Catalyst	Ni (at%)		Mg (at%)		Si (at%)		O (at%)		Mg(at%)/Ni(at%)			Si(at%)/Ni(at%)		
	EDX	XPS	EDX	XPS	EDX	XPS	EDX	XPS	EDX	XPS	XPS-EDX	EDX	XPS	XPS-EDX
A	24.9	15.6	8.2	5.4	8.3	7.3	58.6	71.5	0.329	0.346	0.017	0.333	0.468	0.135
B	26.0	15.5	9.0	5.5	8.0	7.2	57.0	71.7	0.346	0.354	0.008	0.308	0.464	0.156
C	29.5	17.9	8.0	4.6	8.2	6.6	54.3	70.9	0.271	0.257	−0.014	0.278	0.369	0.091
D	35.3	18.3	9.5	5.3	8.6	6.1	46.6	70.3	0.268	0.289	0.021	0.244	0.333	0.089

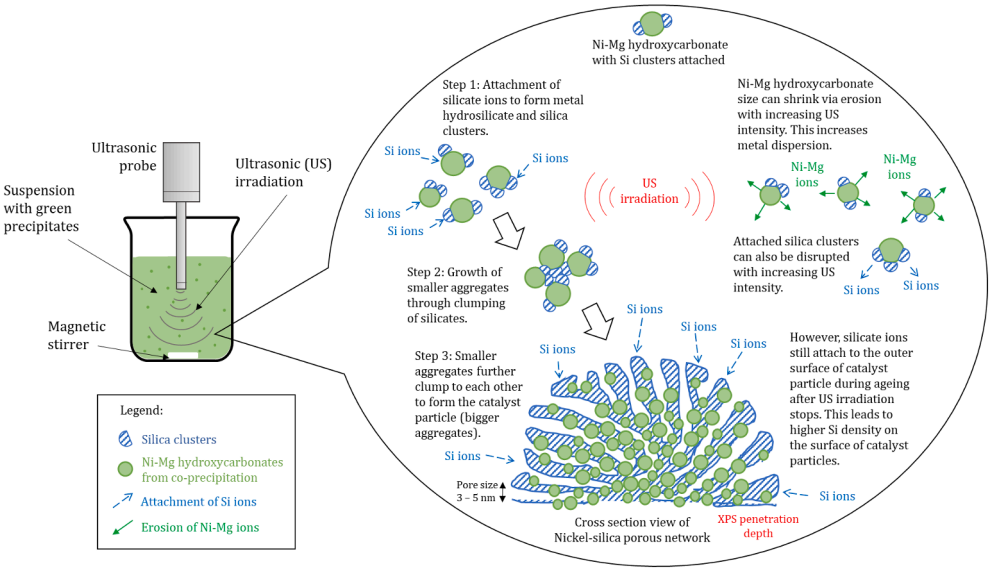

Fig. 2. Conceptualisation of the formation of the nickel-silica porous network during the ultrasound-assisted synthesis of the catalysts.

Table 4
H_2-TPR and H_2-pulse chemisorption results for samples A, B, C and D.

Catalyst	Peaks (Temperature, °C; Relative percentage, %)			Ni metal dispersion[a] (%)	Ni surface area[b] (m^2/g_{Ni})	Particle diameter[c] (nm)
	α	β	γ			
A	181.4	422.2	501.7	8.79	58.55	11.51
	6.2	32.1	61.7			
B	190.6	411.7	495.7	10.26	68.31	9.24
	3.9	35.8	60.3			
C	198.1	418.3	498.7	14.26	94.95	7.10
	3.2	42.5	54.3			
D	190.6	418.2	514.4	17.81	118.53	5.69
	5.2	41.4	53.4			

[a]Calculated according to Eq. (5).
[b]Calculated according to Eq. (6).
[c]Calculated according to Eq. (7).

compared to Ni. It is noted that Ni has a surface energy of 2.080 J/m^2, while Mg has a surface energy of 0.688 J/m^2 [46]. As a result, it is quite likely that a significant amount of Mg was eroded away from the surface layers of Ni-Mg hydroxycarbonate co-precipitates when the ultrasonic intensity was increased. As shown in Table 3, the difference in the Mg/Ni ratio for the surface and bulk (XPS – EDX) decreased as the ultrasonic intensity increased from samples A – C, indicating the increased extent of Mg erosion from the catalyst surface. However, sample D registered an increase in the Mg/Ni ratio difference between the surface and bulk, likely due to the re-attachment of the Mg ions at higher ultrasonic intensities, as similar investigations reported the inefficiency of ultrasonic irradiation at high powers causing the re-agglomeration of particles [47]. In a similar manner, higher ultrasound intensity has also disrupted the formation of hydrosilicates and silica clusters and led to the drop in the bulk Si/Ni ratio, from 0.333 to 0.244.

Following the attachment of silicate ions to form metal hydrosilicate and silica clusters, the individual silicate-attached Ni-Mg hydroxycarbonates would clump together through the -O-Si-O- bonding provided by silicate ions in the ageing solution [45,48]. Small aggregates begin to form from the clumping of nano-sized silicate-attached Ni-Mg hydroxycarbonates (Step 2 of Fig. 2), while further clumping of small aggregates lead to bigger aggregates, eventually forming the catalyst particle network (Step 3 of Fig. 2). The significantly higher Si/Ni ratios as observed by XPS (from 0.468 to 0.333) compared to EDX (from 0.333 to 0.244) was mainly a result of silicate ions attaching to and growing on the outer surface of the aggregated catalyst particles as silica clusters. Attachment of silicate ions within the pores of the catalyst particles is thought to be insignificant compared to the outer surface due to slower mass transfer in the narrow pores. In the present work, ultrasound irradiation was only active during the first 10 min of the ageing process for the sonicated samples, while the remaining ageing period was carried out without ultrasonic irradiation. As higher surface Si/Ni density was also observed for catalyst samples sonicated with high intensity, it can be inferred that the growth of silicate ions on the surface of the catalyst particles took place predominantly following the termination of irradiation, since a high ultrasonic intensity can disrupt the formation of hydrosilicate and silica clusters. It should be noted that the discrepancy between the bulk and surface layer Si/Ni ratios in this present work was in stark contrast with the typical synthesis method of simultaneously co-precipitating the active and support phases. Compared to the sequential precipitation method used in this work, whereby the support phase was added after the co-precipitation of active phases, the simultaneous co-precipitation of both active and support phases could result in a more uniform and homogeneous distribution of the elements [49,50], thus the clustering of the elements would be less drastic in that case.

The XRD diffractograms for the catalysts are shown in Fig. 3. Peaks representing the phases of NiO (ICDD: 01-073-1523), MgO (ICDD: 01-089-7746) and nickel silicate ($Ni_3Si_2O_5(OH)_4$) (ICDD: 01-083-1648) were detected. Diffraction patterns of all samples exhibit reflections at the 2θ value of 36°, 43°, 63°, 75° and 79°, which correspond to NiO (111), NiO(200), NiO(220), NiO(222) and Ni(311) planes, respectively [51,52]. These results agreed well with those of several other investigations [53,54]. The SiO_2 support was amorphous, which did not contribute to any peaks on the diffractogram [55,56]. The NiO crystallite size was ascertained using the Scherrer equation, referencing the characteristic peak at 43°, with the results presented in Fig. 3. In general, the diffractograms registered reflections that appeared broad, which signified the poorly crystallised state of the catalysts. This also indicated

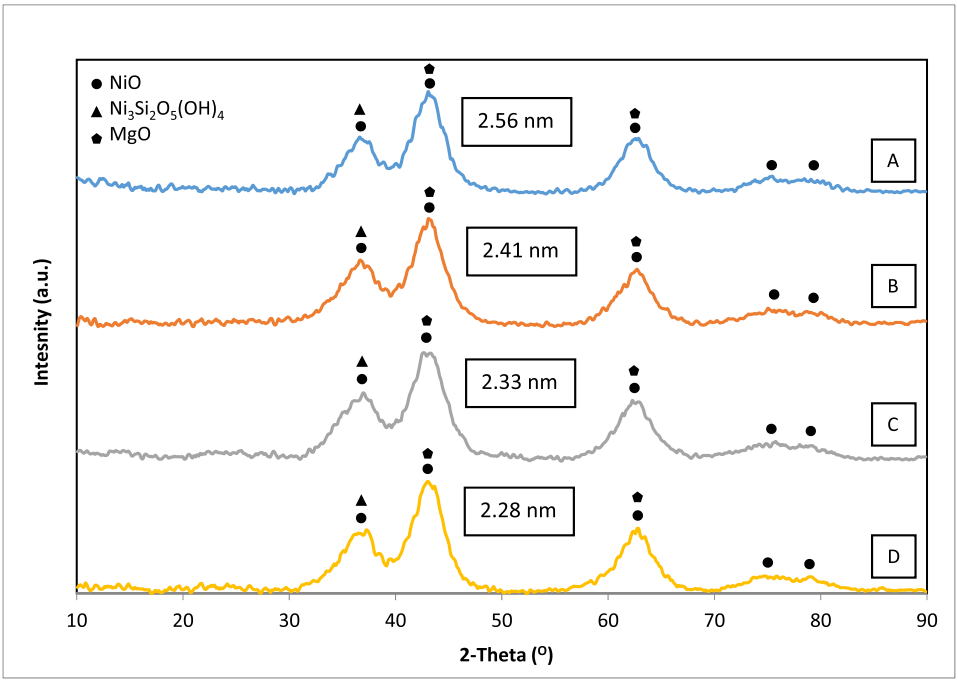

Fig. 3. XRD diffractograms of the unsonicated catalyst A and sonicated catalysts B, C and their respective identified compounds. Note: Insets represent the crystallite size of NiO obtained using the Scherrer equation based on the XRD diffractograms.

the presence of small and well-dispersed phases and highly developed surfaces [57,58]. In addition, the lack of sharp peaks also indicated the absence of large crystalline domains or metal oxide clusters, which could be of great advantage for metal dispersion during catalyst reduction [59]. On the other hand, the presence of nickel silicate, formed by a strong interaction between Ni and Si, is also detected at the 37° peaks. Poorly crystallised nickel silicate compounds with imperfect nickel antigorite structures are commonly formed when the co-precipitating nickel salt and silicate solutions are at temperatures lower than 100 °C, with structures such as $Ni_3Si_2O_5(OH)_4$ [60]. Due to the incorporation of ultrasound during synthesis, the samples registered an increase in amorphicity, evidenced by the decrease in crystallite size of 2.56 nm for the unsonicated catalyst, to a range of 2.28 – 2.41 nm, for the sonicated catalysts. Pertaining to the sonicated catalysts, the crystallite size decreased with the increase in ultrasonic intensity. This may be owed to the highly turbulent mixing induced by sonicating the suspension during synthesis, in which unique conditions due to acoustic cavitational bubble collapse were produced. This highly turbulent mixing is facilitated by the presence of acoustic streaming and high mass transfer [61] and subsequently resulted in a higher packing disorder in the samples, forming samples that were more amorphous [25]. Furthermore, as the cavitation bubbles collapsed violently, localised regions of extremely high cooling rates, in the range of 10^{11} K/s, were generated, which could inhibit the growth of crystals [25].

H_2-TPR was used to probe the redox properties of the unsonicated and sonicated catalysts, with results presented in Fig. 4. The reduction profiles of the catalysts are characterised by multiple reduction peaks fused together into a much broader reduction band from 100 to 800 °C, with a peak ca. 400 – 500 °C. This observation denotes the homogeneous distribution of small particles over the support, with the presence of complex and intimate interactions between the active phase and support, which supports the XRD diffractograms and is also in accordance with other researchers [6,45,57,62], as well as Ni catalysts prepared via other techniques such as sol–gel [63]. From the figure, it is observed that the unsonicated catalyst had the highest maxima of 448.9 °C, while the sonicated catalysts had maximum reduction peaks in the range of 431 – 435 °C. Moreover, sample D, irradiated with the highest ultrasonic intensity presented the lowest reduction peak at 431.4 °C. The presence of ultrasound during synthesis has marginally increased the reducibility of the catalysts, which is also a finding supported by other relevant investigations concerning ultrasound-assisted catalysts synthesis [29,64]. The increase in reducibility also signified the decrease in extent of metal-support interactions, in which phases with weaker interaction with the support (i.e. NiO) would be more readily reduced to Ni^0.

To gain more insight into the TPR results, the broad peaks were deconvoluted into symmetrical peaks via Gaussian multipeak curve-fitting to evaluate the relative percentage of the different reducible species, as well as their peak positions, presented in Fig. S1 (Supplementary information). In total, three main peaks could be identified, which were labelled as α, β and γ. The reduction temperatures reported can be classified into different types of nickel species, which are directly associated with the degree of interaction with the silica support. This also indicates that Ni species of different extents of interaction coexist within a catalyst sample. Henceforth, the three peaks are classified based on their reducibility and explained based on their relative proportion and individual peak position. It is noted that no reduction peaks corresponded to the reduction of Mg species due to their extreme difficulty in reduction under the present conditions applied [59]. The first low temperature peak (α) at ca. 181 – 198 °C represented a minor portion approximately 6% or less of the total reduction profile. These are ascribed unambiguously to the reduction of higher Ni(III) oxides in trace quantities (Ni_2O_3 to NiO), which is a common occurrence for precipitates calcined at temperatures 400 °C or lower, as per this present study [13,63]. However, since the XRD results exhibited no obvious Ni_2O_3 signals, it is suggested that the Ni_2O_3 phase present was too sparse in amount and also highly dispersed on the support [52]. On the other hand, the β peaks at ca. 411 – 422 °C were due to the NiO species possessing weak interactions with the silica support [65,66]. Lastly, the γ peaks at ca. 495 – 514 °C were due to the Ni species having strong interactions with the silica support, hence forming Ni silicate, which presented difficulty in reduction [65,66].

Based on Table 4, one can see that the composition of α for all

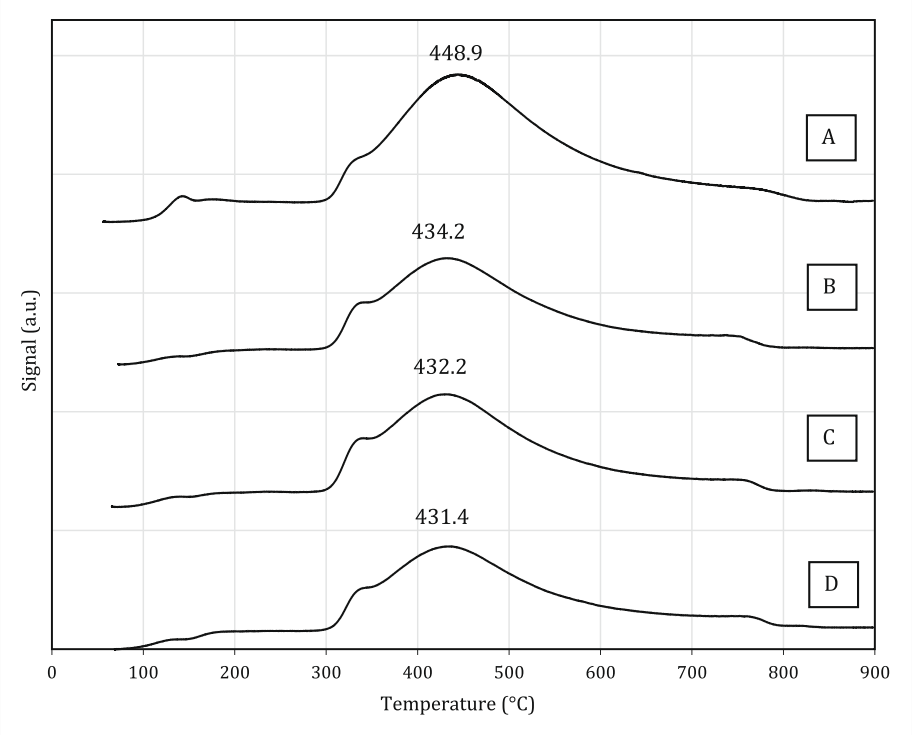

Fig. 4. TPR profiles at temperatures 30 – 900 °C obtained for samples A, B, C and D.

samples remained in the range of approximately 3–6%, representing their minor role in the catalysts. However, the percentages of β and γ varied significantly with the presence of ultrasound and its intensity. In general, the weaker NiO phase, β, observed an increase in proportion with the increase in ultrasound intensity, from 32.1% in the unsonicated catalyst and up to 42.5% in the sonicated counterparts. Accordingly, the Ni phase with stronger interactions, γ, also observed a declining trend with the increase in ultrasound intensity, registering 61.7% in the unsonicated catalyst and down to 53.4% for sample D, which suggests the possibility of Ni silicate erosion or inhibition by ultrasonic irradiation. Interestingly, the increase in ultrasonic intensity from 20.78 to 27.72 W cm^{-2} did not lead to significant variations in the relative percentages of β and γ, which indicates that there is a limit to the extent of Ni silicate erosion caused by ultrasonic irradiation. Considering the bond linkages of -Si-O-Ni- present in Ni hydrosilicate species [45] and the bond dissociation energy of Ni-O as 391.6 kJ mol^{-1} [67], calculations have shown that it is in fact plausible for acoustic micro-bubble implosions to generate sufficient energy for the bond breakage of Ni-O [68], which erodes away the Ni hydrosilicate structure.On the other hand, with a significantly higher bond dissociation energy at 440 kJ mol^{-1} for the Si-O bonds present in the bond linkages of -Si-O-Si-, it became more difficult to instigate bond breakage once silicate ions were attached to the hydrosilicates to form silica. Consequently, this allowed the silica clusters to act as a protective layer, enclosing the Ni silicate phases to impede its erosion caused by ultrasonication. Instead of Ni silicate erosion, it appeared that the increasing ultrasonic intensity has caused considerable agitation that suppressed the build-up of silica clusters by deterring the polymerisation of silicic acid [69], leading to the decreasing trend of Si/Ni ratios as shown previously in Table 3.

Apart from the compositional change in Ni phases in the catalyst, the increase in ultrasonic intensity has also resulted in the shrinkage of Ni-Mg hydroxycarbonate nanoparticles, leading to higher Ni surface area and dispersion. In particular, Ni dispersion was increased from 8.79% to 17.81%, while the Ni surface area was increased from 58.55 m^2/g_{Ni} to 118.53 m^2/g_{Ni}, as seen in Table 4. This suggested that Ni was more dispersed across the support due to the action of ultrasonic irradiation during synthesis, whereby the increase in intensity amplified this phenomenon. As discussed earlier, the improvement in Ni dispersion and surface area could be due to the erosion of Ni-Mg hydroxycarbonates caused by ultrasound irradiation, with higher intensity lead to more severe erosion. Given that the pH remains unchanged at 8.8 during the application of ultrasound irradiation, it is thought that the eroded Ni and Mg ions would re-precipitate and form smaller hydroxycarbonate nanoparticles, which in turn lead to higher Ni dispersion and Ni surface area. Generally, the increase in total metal surface area and dispersion are good indicators of enhanced catalytic activity, as more active sites equate to more area available for reaction to occur.

The chemical and electronic properties of the calcined catalysts were studied using XPS. As per Fig. 5, the spectra show features associated with Ni $2p_{3/2}$. For all catalysts, the Ni $2p_{3/2}$ is accompanied by the presence of a satellite peak at 861 – 863 eV, congruous to the existence of Ni^{2+} instead of metallic Ni^0 [70]. It is noted that these satellite peaks manifest due to the paramagnetic state of the Ni^{2+} species and electron shake-up. Notably, these peaks are typically ca. 6 eV higher than the main Ni $2p_{3/2}$ peak [71], as noted by the ΔE_{sat} values in Table 5.

The Ni $2p_{3/2}$ binding energy of the unsonicated catalyst resonated well with reported values of 856.3 – 856.7 eV [72,73]. However, it is discovered that the Ni $2p_{3/2}$ binding energy of the sonicated catalysts experienced a shift to lower values at 855.7 – 855.9 eV. Since XPS analysis is surface sensitive, the discrepancies in binding energies indicated that the Ni species on the surface have been altered electronically [2], in this case due to the incorporation of ultrasound into the synthesis procedure of the catalysts. Furthermore, a decrease in binding energy also indicated a lowered extent of metal-support interaction between the Ni phase and Si phase [2,74]. In this case, a shift to lower binding energies due to ultrasound has also been reported by other researchers [75], which led to a change in electron density that may affect the bonding of chemical intermediates to the active sites, thus ultimately affecting the reaction pathways during hydrogenation [76–78]. Furthermore, this indication of weakening in metal-support interactions is also corroborated with the TPR studies demonstrated earlier, noting the shift in main reduction peaks to lower temperatures in sonicated

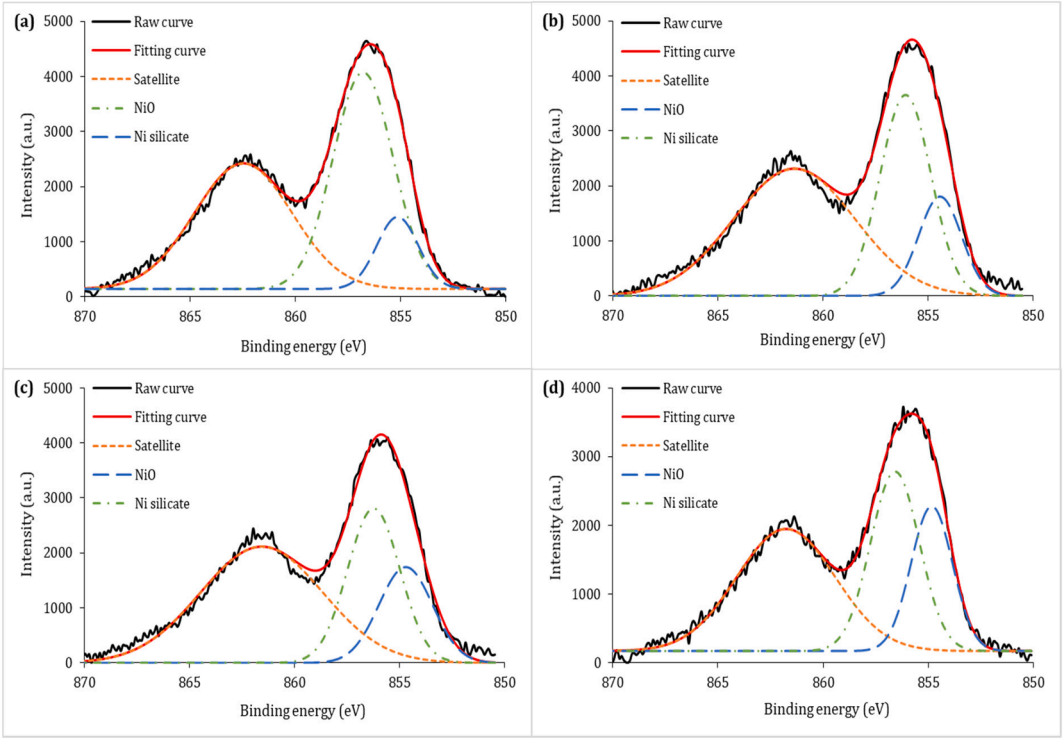

Fig. 5. Ni $2p_{3/2}$ XPS spectra fitting for (a) catalyst A; (b) catalyst B; (c) catalyst C and (d) catalyst D.

Table 5
XPS analysis results for catalysts A, B, C and D.

Sample	Ni $2p_{3/2}$ (eV)	Ni $2p_{3/2}$ satellite (eV)	ΔE_{sat} [a] (eV)	Fitted peaks (eV)		Relative proportion[b] (%)		Si 2p (eV)	$\Delta E^{c}_{Ni\text{-}Si}$ (eV)
				NiO	Ni Silicate	NiO	Ni Silicate		
A	856.64	862.48	5.84	855.15	856.79	18.6	81.4	103.2	753.44
B	855.78	861.37	5.59	854.44	856.08	29.5	70.5	103.6	752.18
C	855.84	861.57	5.73	854.72	856.24	38.8	61.2	102.5	753.34
D	855.83	861.76	5.93	854.83	856.58	40.7	59.3	102.1	753.73

[a]Separation of Ni $2p_{3/2}$ primary line to satellite.
[b]Ratio of integrated area of the two compounds via curve fitting.
[c]Difference between Ni $2p_{3/2}$ and Si 2p.

samples.

To gain more insight into the XPS results, the Ni $2p_{3/2}$ XPS core level region was deconvoluted via Gaussian multi-peak curve-fitting and fitted with three doublets assigned to NiO, Ni silicate and associated satellite features, as shown in Fig. 5. As the NiO binding energies have been reported to be significantly lower at a range of 854 – 855 eV [72,73,79], it is suggested that another Ni phase exists at a higher binding energy, which is assigned to the Ni silicate phase. Hence, this agreed well with the two Ni phases detected in the XRD and TPR analyses. In addition, it is known that a relationship can be derived using the difference between Ni $2p_{3/2}$ and Si 2p binding energies, $\Delta E_{Ni\text{-}Si}$ [80]. The existence of Ni silicates in the catalyst sample would give $\Delta E_{Ni\text{-}Si}$ values of 753.2 – 753.8 eV [73,81,82]. From Table 5, the $\Delta E_{Ni\text{-}Si}$ values of the catalysts synthesised agreed excellently with this, thus substantiating the presence of the aforementioned phases. Literature has also reported similar binding energy values of nickel silicates [73].

The total area of respective signals, when averaged over the whole system, allows one to approximate the relative amount of species considered [83]. In this case, the area under the curve of each deconvoluted peak in Fig. 5 were used to estimate the relative surface proportion of each nickel species, which are presented in Table 5. Echoing the results from the TPR analysis, sonication has also imparted considerable discrepancies on the NiO and Ni silicate surface compositions. The proportion of NiO on the surface was increased from 18.6% in the non-sonicated catalyst to 29.5 – 40.7% in the sonicated catalysts, in which this proportion has also increased with higher ultrasonic intensities. Conversely, the Ni silicate phase has also seen a decrease in relative proportion when ultrasound was used during the synthesis, as it dropped from 81.4% in the unsonicated catalyst to a range of 59.3 – 70.5% in the sonicated counterparts. This aforementioned trend observed in the XPS analysis was similar to those obtained from the TPR analysis, albeit with a greater magnitude of change. This was due to the fact that XPS presents details on surface composition, which could vary slightly from those of the bulk provided by TPR measurements [84].

It was reported that the precipitation of silicates without the use of surface modifiers tend to clump to each other, which results in the formation of secondary aggregates [48], hence in the case of no sonication (samples A) and low power sonication (sample B), silicate ions would adhere to existing silicate networks in an unperturbed manner during suspension ageing, resulting in a higher degree of aggregation within a shorter period of time. With such a phenomenon, the relatively unhindered growth of the silicate network is more prominent, which brought about longer and more severe ageing conditions on the outer surface of the catalyst particles for samples A, as validated by the XPS analysis showing the high concentration of Ni silicates on the surface (81.4%). As opposed to the above case, the inclusion of ultrasonic irradiation during support loading and the early stage of ageing could effectively disperse the aggregates and suppress the growth of the catalyst particles, mainly by delaying the growth of the silicate network. The erosion caused by high intensity ultrasonic irradiation coupled with the delayed growth of silica on the outer surficial layers eventually limited the extent of ageing, as exhibited by the lower Ni silicate concentration in samples C (61.2%) and D (59.3%). Such a delayed growth in particles could have also played a role in enhancing the Ni dispersion in sonicated catalysts, as smaller particles result in an increase in total exposure of Ni active sites. Herein, the conceptualisation of the two different states of ageing is shown in Fig. 6.

The textural and structural properties of the calcined nickel catalysts were evaluated using N_2 physisorption, in which the adsorption–desorption isotherms for the catalysts can be seen in Fig. S2 (Supplementary information). According to the IUPAC classification, the sonicated samples (B – D) exhibited Type IV(a) isotherms, characteristic of mesoporous substances with capillary condensation accompanied by hysteresis. Contrariwise, the non-sonicated sample A exhibited a hybrid of the Type II and Type IV(a) isotherms, denoting the presence of mesopores and macropores, which was also accompanied by a hysteresis loop. Regarding the hysteresis loops exhibited by the catalysts, they can be ascribed to the Type H2(b) hysteresis loop, which signifies the presence of ink-bottle pores with a wider size distribution of neck widths, typical of mesoporous ordered silicas obtained after hydrothermal treatment [85].

The incorporation of ultrasound is said to have altered the textural properties of the catalyst, resulting in more uniform mesoporous structures with higher BET surface areas, as shown in Table 6. The increase in surface areas was also noted in other studies, in which ultrasound acted as a dispersant tool for catalyst phases, which might increase the total surface area available for reaction [36,64]. The imploding microbubbles in the irradiated suspension as a result of acoustic cavitation facilitated the nucleation and fine dispersion of particles, creating phases of more uniform and well-defined morphology that resulted in increased surface areas from 192.5 m^2/g to a range of 228.9 – 289.7 m^2/g [86]. According to Coenen [87] and Ghuge et al. [45], it is the nickel antigorite (hydrosilicate) phase instead of the silica support that gives rise to a high BET surface area, with the former typically exhibiting >300 m^2/g while the latter presenting surface areas in the range of 20–50 m^2/g. If one is to refer to the results from the TPR studies (Table 4), it can be assumed that sample A with the highest Ni silicate percentage (61.7%) would exhibit the highest BET surface area. However, Table 6 shows otherwise with sample A exhibiting a significantly lower BET surface area compared to the sonicated samples. As discussed earlier, the amount of silica clusters attached to the hydrosilicate declined with the usage of ultrasound, which in turn led to higher hydrosilicate to silica ratio in the samples synthesised with ultrasonic irradiation, thus giving rise to a higher BET surface area. In fact, this observation is also correlated with the increase in ultrasonic intensity from sample B – D, whereby the formation of more silica clusters were suppressed, causing a further increase in hydrosilicate to silica ratio, thereby progressively increasing the BET surface area as per Table 6. As a result, sonicated catalysts exhibited higher range in the overall BET surface area than the unsonicated catalyst. Nevertheless, the pore volume and average pore width of the catalysts were similar in range, noting that the non-sonicated sample possessed a larger average pore width due to the presence of macropores, which can also be observed in the pore size distribution in Fig. 7. One can see that all samples had a uniform pore size distribution in the mesoporous range, while the non-sonicated sample also contained pores in the macroporous range. The

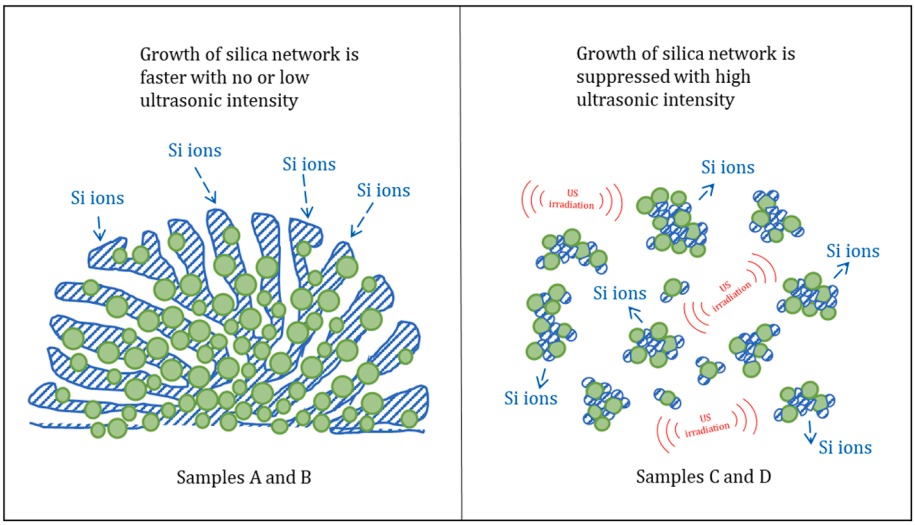

Fig. 6. Status of nickel-silica network/particles upon first 10 min of ageing with and without ultrasonic irradiation.

Table 6
Textural properties of calcined catalysts from N_2 physisorption.

Catalyst	BET surface area ($m^2\ g^{-1}$)	Pore volume[a] ($cm^3\ g^{-1}$)	Average pore width[a] (nm)	Relative pore flow rate[b]
A	192.5	0.2277	4.85	1.964
B	228.9	0.2241	3.46	1
C	258.6	0.2169	3.74	1.168
D	289.7	0.2515	3.70	1.144

[a]BJH desorption branch.
[b]Calculated based on the Q α (pore width)^2 relationship from the flow continuity equation. It is assumed that all other parameters remain unchanged.

presence of larger macropores is likely due to the unperturbed and prolonged ageing [88,89] relative to that experienced by the sonicated catalyst, which contributed to the increase in average pore width for catalyst A. Overall, the presence of pores above 3.5 nm was a good indication that the catalysts were suitable for the hydrogenation of edible sunflower oil, which are approximately twice the size of the triglyceride molecules of 1.5 – 2 nm [8,44]. However, the presence of narrower pores with average width slightly below 3.5 nm in catalyst B might have posed significant diffusional and mass transport problems for the movement of triglycerides. Table 6 collates the relative pore flow rate for each catalyst, with catalyst B as the reference. Employing the flow continuity equation, it is inferred that the unsonicated catalyst A had a 96.4% higher flow rate than sample B. The smaller flow area due to smaller pores denote the increased hindrance in mass transfer, which results in the slower diffusion rate of reactants and products in and out of the pores, leading to decreased activity relative to samples possessing higher pore flow rates.

3.3. Catalytic performance of synthesised catalysts

3.3.1. Hydrogenation activity

All synthesised catalysts were subjected to catalytic activity tests via the partial catalytic hydrogenation of sunflower oil. The decline in IV throughout the stipulated reaction time of 90 min for each catalyst sample was noted and presented in Fig. 8. The hydrogenation performance was tracked by observing the decrease in the IV. The sunflower oil utilised as the reactant has an initial IV of 124, which was tested with the above-mentioned iodine value test. As anticipated, the IV for all sample sets decreased as the reactant was progressively saturated during hydrogenation. Furthermore, the gradient of the graph signified the rate of decline in the IV, whereby a sharper gradient represented an increase

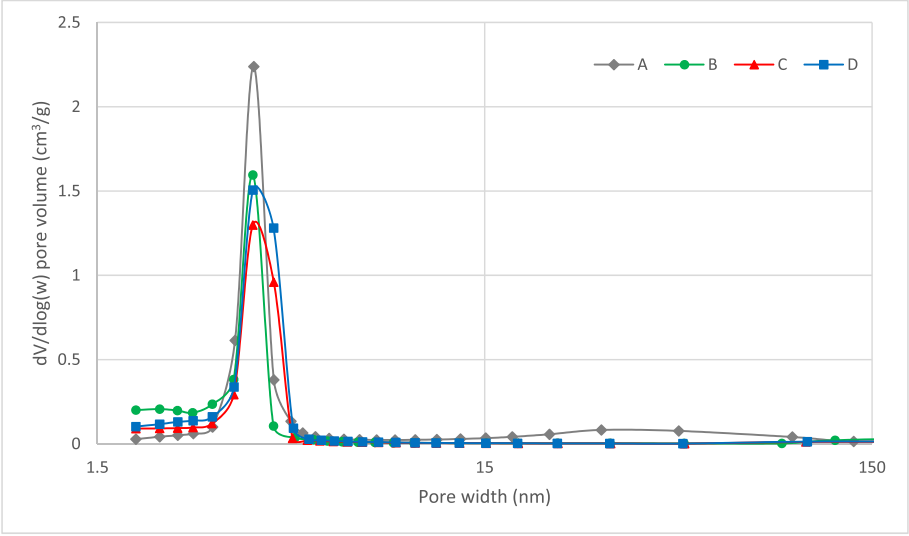

Fig. 7. Pore size distributions obtained for the unsonicated catalyst A and sonicated catalysts B, C and D.

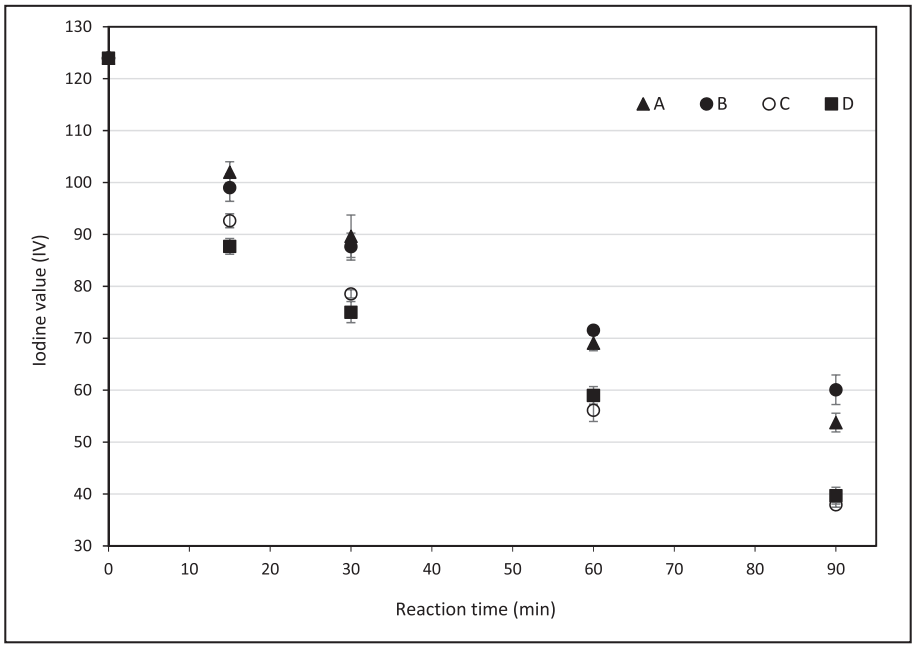

Fig. 8. Change of iodine value (IV) over time using different catalyst samples over the course of partial hydrogenation using sunflower oil. Note: Error bars indicate data replication in triplicates performed for the iodine value tests.

in hydrogenation activity. Catalyst C, synthesised with an ultrasonic intensity of 20.78 W cm^{-2} registered the highest activity among the catalysts synthesised, attaining a final IV of 37.9 after a reaction time of 90 min. On the other hand, the unsonicated catalyst produced an IV drop to 53.8 in 90 min. The least active catalyst was catalyst B, synthesised with an ultrasonic intensity of 7.07 W cm^{-2}. Although possessing higher

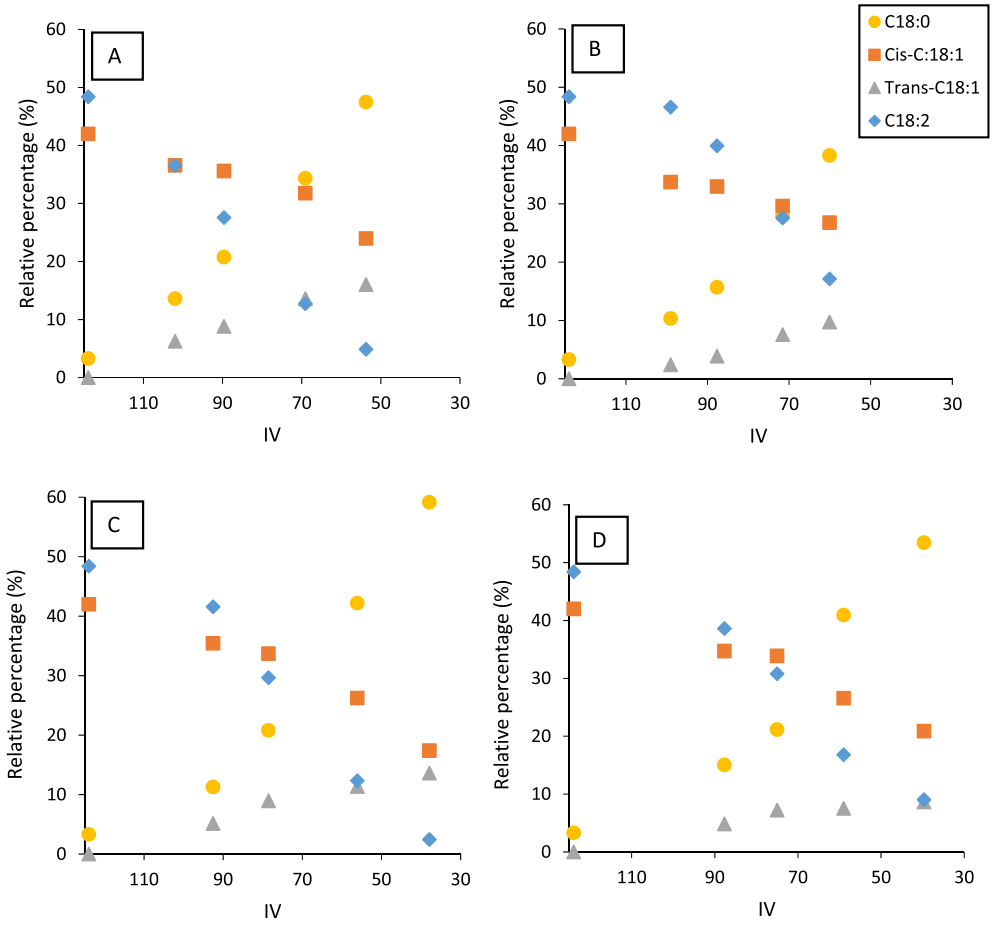

Fig. 9. Evolution of fatty acid compositions with the iodine value (IV) during the partial hydrogenation reaction using catalysts A, B, C and D.

Ni surface area and dispersion than its unsonicated counterpart, catalyst B presented a smaller pore size below 3.5 nm. Coenen [7] postulated that while it is beneficial to possess a high Ni dispersion and surface area, oil/fat hydrogenation is also structure-sensitive, whereby pores narrower than 3.5 nm would considerably impair the mass transport and pore diffusivity of bulky triglyceride molecules, hence causing pore congestion and affecting overall catalytic activity. The initial activity of catalyst B was higher than that of catalyst A due to its advantages in Ni dispersion and surface area. However, at IV = 90, the activity of catalysts A and B began to diverge as shown in Fig. 8, the percentage of bulky triglyceride molecules (C18:2 and *cis*-C18:1) for sample B remained relatively high compared to that of sample A, as shown in Fig. 9. As the narrower pores in sample B effectively impede the diffusion of these molecules, the reaction and conversion of such molecules would be affected negatively, thus resulting in a slower drop in IV. In addition, as presented in Table 6, the unsonicated catalyst A has a 96% higher flow in the pores than that of catalyst B, indicating that despite a higher intrinsic catalytic activity possessed by catalyst B, its mass transfer at the pores was severely impacted thus affecting the overall catalytic activity.

Based on the catalyst characterisation results, the geometric effects imparted by ultrasonic irradiation have led to the sonicated catalysts possessing superior catalytic activity compared to their unsonicated counterpart, with the exception of the sonicated catalyst B due to its disadvantages in pore characteristics. The action of ultrasound during synthesis has induced the formation of more reducible Ni species available on the catalyst superficial layers, which on the other hand are composed of particles of lower agglomeration, thus leading to increased Ni surface area and dispersion after reduction. The presence of more well dispersed active sites ultimately allowed more reactants and intermediates to adsorb and react. Nevertheless, it was also discovered that catalyst D, albeit sonicated with the highest ultrasonic intensity, performed marginally poorer than catalyst C, whereby the hydrogenation activity of the latter overtook the former during mid-hydrogenation. This could be due to the large Ni surface area exhibited by catalyst D, allowing more surface area contact with the reacting medium, hence increasing the propensity of Ni lixiviation. Indeed, AAS analyses performed on the hydrogenation products of catalysts C and D confirmed that the concentration of Ni present in the hydrogenation product of catalyst D was ca. 30% higher than that of catalyst C at 90 min (0.00294 mg Ni/g oil vs. 0.00226 mg Ni/g oil), which caused the gradual deactivation of catalyst D over time.

3.3.2. Hydrogenation selectivity and product distribution

The hydrogenation activity of the synthesised catalysts was demonstrated via the IV tests, which is a direct representation of the number of carbon–carbon double bonds present in a sample, without any discrimination towards the product composition. Product analyses are also very crucial in distinguishing the behaviour of catalysts during edible oil hydrogenation. The synthesised catalysts were appraised by monitoring the evolution of saturated fat (C18:0), *trans*-C18:1 and *cis*-C18:1 at particular IV levels which represent a reaction time up to 90 min, as depicted in Fig. 9. The respective yield and selectivity of the catalysts are shown in Table 7.

From Fig. 9 it can be seen that the composition profile of the hydrogenated fats depicted similar trends for all catalysts used. The elimination of carbon–carbon double bonds, as well as *cis–trans* isomerisation during hydrogenation can be tracked throughout the plots. Overall, a depletion of C18:2 and increase in C18:0 is observed, accompanied by a variation of *cis*-C18:1 and *trans*-C18:1 composition throughout the reaction. Another observation was the overall increase in *trans*-C18:1 coupled with the overall decrease in *cis*-C18:1 for all hydrogenation runs. It has been documented that *trans*-C18:1 are preferentially formed during the initial phase of hydrogenation [90]. On the other hand, *cis*-C18:1 was either isomerised to *trans*-C18:1 or fully hydrogenated to C18:0. It can be seen that the formation of *trans*-C18:1 was generally less favoured in the hydrogenation runs using sonicated

Table 7
Yield and selectivities of catalysts for the sunflower oil hydrogenation reaction.

	trans-C18:1 yield (%)		C18:0 yield (%)		C18:0/*trans*-C18:1 selectivity (%) [a]		*trans*-C18:1/*cis*-C18:1 selectivity (%) [b]	
IV	90	70	90	70	90	70	90	70
A	9.68	15.1	22.6	36.6	70.0	70.8	20.5	30.4
B	4.30	8.70	16.1	31.5	79.0	78.4	10.8	21.6
C	5.38	10.8	12.9	30.1	70.6	73.7	12.5	24.4
D	4.26	7.61	13.8	31.5	76.5	80.6	10.0	18.4

[a]Calculated with $\frac{C18:0 yield(\%)}{C18:0 yield(\%) + trans C18:1 yield(\%)} * 100$.

[b]Calculated with $\frac{trans C18:1 yield(\%)}{trans C18:1 yield(\%) + cis C18:1 yield(\%)} * 100$.

catalysts, whereby the selectivity of *trans*-C18:1/*cis*-C18:1 at IV 90 and 70 were at the lower range of 10 – 12.5% and 18.42 – 24.39%, respectively. Meanwhile, the unsonicated catalyst presented higher *trans*-C18:1/*cis*-C18:1 selectivities of 20.46% and 30.43% at IV 90 and 70, respectively.

While Fig. 9 gives a useful outline of the catalytic performance of each sample over the course of the reaction, it is also highly crucial to analyse the product distribution correlated to a specific target IV. In particular, the concentration of *trans*-C18:1 and C18:0 are of paramount significance in deciding the final oil quality. Fig. 10 demonstrates the percentage of C18:0 and *trans*-C18:1 fatty acids at an IV of 70. In this case, this particular level was chosen for comparison as it is a common target IV for oleomargarine products and it also corresponds to the point where the formation of C18:0 starts to be significant [6]. This extent of hydrogenation resembles to that in the manufacture of fatty acid components required for shortenings and margarine in the industry [91]. Employing the sonicated catalysts, the hydrogenation products obtained at an IV of 70 presented *trans*-C18:1 at equal to or less than 10%, while the hydrogenation products of the unsonicated counterpart registered *trans*-C18:1 levels of 13.7%, with the lowest *trans*-C18:1 level observed using catalyst D. On the other hand, the sonicated catalysts had similar percentages at approximately 29% in C18:0 production, while the unsonicated catalyst was slightly higher at 34%.

Generally, as the overall hydrogenation proceeded, the isomerisation of fatty acid products increased with conversion. However, it is noted that the mechanisms related to hydrogenation and *cis/trans* isomerisation are heavily interlinked. With regards to the formation of *trans* fatty acids (TFAs) during hydrogenation, the addition–elimination mechanism proposed by Horiuti and Polanyi [92] is commonly adopted to illustrate the process. The mechanism states that both the hydrogenation and isomerisation processes are governed by a half-hydrogenation state mechanism. Firstly, carbon–carbon double bonds of C18:2 or C18:1 molecules are adsorbed on active sites. It is noted that C18:2 bonds tend to adsorb to the surface to a stronger degree and are thus first hydrogenated. Therefore, this also explains the consecutive drop in linoleic content throughout the reaction as per Fig. 9. After adsorption, one of the double bonds are half-hydrogenated by the addition of one hydrogen atom from the active sites. Further reaction resulting in the saturation of C–C bonds necessitates the addition of another hydrogen atom. Nevertheless, typically without the presence of a second hydrogen atom, the first hydrogen atom detaches from the half-hydrogenated intermediate, thus re-establishing the double bond with either a *cis*-C18:1 or *trans*-C18:1 configuration [56]. Particularly, the latter configuration is more thermodynamically favoured than the former [93]. As hydrogenation is supplemented by isomerisation reactions, it is suggested that the change in the electronic characteristics of the sonicated Ni catalysts could also influence the isomerisation reactions. In this case, the enhanced removal of the chemisorbed half-hydrogenated intermediate from the active sites could prevent the further isomerisation to TFAs. This alteration in electronic properties may be used to explain the decrease in TFA formation for the sonicated

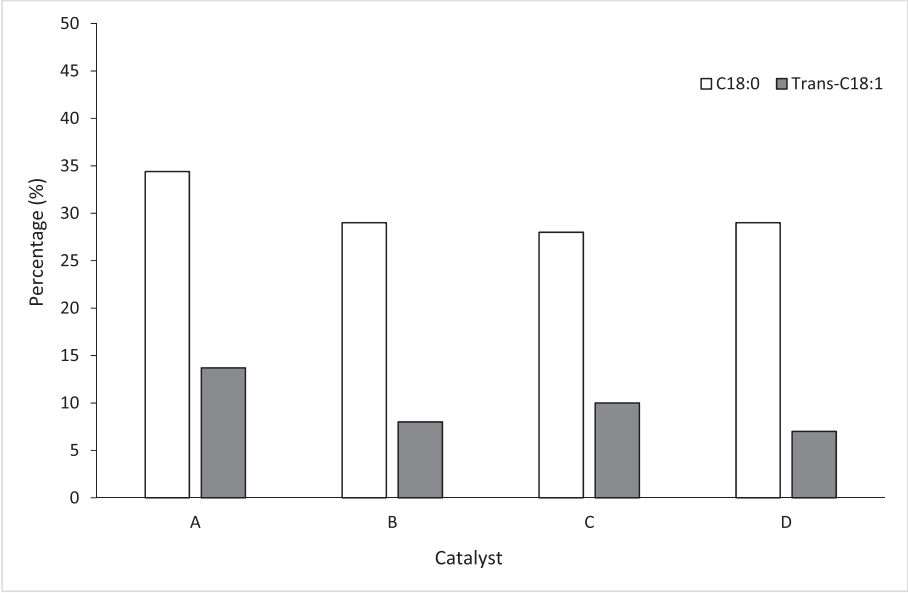

Fig. 10. Percentage of *trans* fatty acids and saturated fatty acids formed at IV = 70 for the samples.

catalysts, relative to the unsonicated counterpart [2,94]. Hence, one of the functions of ultrasound in this case of catalyst synthesis might be as a selectivity modifier for the Ni catalyst. Through sonication, the bonding strength of the adsorbates on the active sites were altered, which resulted in the increase of the energy barrier required for fatty acid isomerisation or the decrease of the energy barrier for hydrogenation that hastens *cis*-C18:1 to C18:0 conversion [94]. In particular, the shift from a higher to lower binding energy in the sonicated catalysts as observed in the XPS results (Table 5) complemented this finding. The changes in the electronic properties and electron densities of catalysts as observed by the shift in binding energies is known to alter the adsorption of reacting species and hence the selectivity towards the final products [95–97]. In this case, the decrease in binding energy denotes the increase in electron density of Ni species on the catalyst surface, thus leading to weaker interactions between the adsorbed or hydrogenated intermediates and the active sites, allowing easier desorption thus diminishing the transformation of unsaturated fat molecules or *cis* isomers to *trans* isomers [98], which was also a phenomenon reported by other researchers such as Iida et al. [99]. Similarly, Li et al. [75] has noticed a negative shift in binding energy for Ru species in Ru-B catalysts after sonication, which facilitated the adsorption of the oxygen atom of carbonyl groups in the cinnamaldehyde molecule, ultimately enhancing the hydrogenation of the molecule.

To further assess the hydrogenation performance of the synthesised catalysts in this work, comparisons to novel catalysts obtained from recent literature were made, with a compilation presented in Table 8. Compared to most studies, it can be seen that catalyst C in this present work was able to achieve an IV drop to 70 in a shorter reaction time of 40 min, while containing a low amount of saturated fats and *trans*-fats, particularly the latter. Although noble metal (e.g. Pt and Pd) catalysts required milder reaction conditions (approximately 100 °C) and produced lesser saturated fats, the present catalyst was able to achieve a relatively low *trans*-fats percentage of 10%. It should also be noted that the saturated fats content for noble metal catalysts were comparatively lower due to their lower extent of reaction. Compared to the other Ni-based hydrogenation catalysts such as Ni/ZnO/Al_2O_3, Ni/SiO_2, Ni-Mg-Ag/D and Ni-Ce/Al_2O_3, the novel sonicated catalyst in this work has produced at least half the amount of *trans*-fats, while maintaining

Table 8
Comparison of the present work to other works obtained from recent literature.

Sample	Temperature and pressure	Initial IV	Final IV	Reaction time (min)	*Trans*-fats (%)	Saturated fats (%)	Oil feed employed	Ref.
Ni/ZnO/Al_2O_3	180 °C 5 bar	162	70	130	22.8	33.5	Sunflower	[94]
Ni/SiO_2	180 °C 4.5 bar	138	70	44	26.1	33.6	Sunflower	[62]
Ni-Mg-Ag/D	160 °C 1.6 bar	130	90	255	26.3	5.8	Soybean	[100]
Ni-Ce/Al_2O_3	180 °C 6 bar	115	70	33	26.4	16.6	Canola	[4]
Pd-Ru/SBA-15	110 °C 5 bar	130	70	60	24.5	16.5	Sunflower	[101]
Pd/γ- Al_2O_3	100 °C 4.2 bar	125	90	20	19.9	5.6	Sunflower	[102]
Pd/SBA-15	110 °C 5 bar	130	80	60	34	10	Sunflower	[103]
Pt-Ni/SiO_2	170 °C 3 bar	130	70	180	16.8	23.2	Sunflower	[56]
Ni-Mg/SiO_2 (unsonicated)	180 °C 5 bar	124	70	59	13.7	34.4	Sunflower	Present work
Ni-Mg/SiO_2 (I_{US} = 20.78 W cm^{-2})	180 °C 5 bar	124	70	40	10	28	Sunflower	Present work

comparable if not better hydrogenation activity. Nevertheless, it should be noted that these studies obtained from the literature were executed with disparities in reaction conditions and oil variation, hence the overall activity and *trans*-fats and saturated fats contents would have also been affected. For instance, the Ni-Ce/Al_2O_3 catalyst although requiring only 33 min of reaction time for hydrogenation, was employed to hydrogenate a feed oil with the lowest initial IV of 115. Therefore, this present work has exemplified the potential of incorporating ultrasonic technology into the synthesis of such Ni hydrogenation catalysts, with positive and applicable end results i.e. the enhancement of hydrogenation activity and the lowering of detrimental *trans*-fats for edible oil applications. For the latter application, edible oil manufacturers and catalyst developers who seek an alternative technique to lower their *trans*-fats production substantially could take the ultrasound-assisted catalyst synthesis procedure into consideration for their processes.

4. Conclusions

This present work was performed to investigate the synthesis of silica-supported nickel catalysts using the ultrasonic technique and its application in the partial hydrogenation of edible oil. It was successfully shown that the incorporation of ultrasonic irradiation into the ageing process of sequentially precipitated catalysts have led to benefits in terms of the catalyst characterisation properties and their performance in the catalytic hydrogenation of sunflower oil. Further understanding into the proposed mechanisms indicated that the usage of ultrasonic irradiation, as well as variations in its intensity, had profound impacts on the overall characteristics and compositions (hydroxycarbonates, silicates and silica clusters) comprising the catalysts. It is noted that ultrasonic irradiation had a significant influence on the ageing properties of the catalysts, which directly affected the formation of silica clusters, followed by hydroxycarbonates and Ni silicates. For instance, ultrasonic irradiation led to the erosion of hydroxycarbonate phases and the suppression of silica clusters, which once formed, serve as protective enclosing to avert Ni silicate erosion. As the ultrasonic intensity was increased, greater Ni dispersion was achieved due to increasing extents in hydroxycarbonate erosion, while increase in BET surface areas was also noted due to the decrease in silica to hydrosilicate ratio as a result of the suppression of silica clusters. On the other hand, it was also observed that upon the termination of ultrasonic irradiation, the growth of the silica network on the surface of the catalysts during ageing also led to a higher Si composition on the external layer of the catalyst particles. In general, these effects in turn imparted alterations to the geometrical and electronic properties of the catalysts, improving catalyst reducibility, surface area and dispersion of the material.

Hydrogenation using the catalyst synthesised at an ultrasonic intensity of 20.78 W cm^{-2} achieved the fastest decrease to IV = 70 in 40 min, compared to 58 min achieved by its non-sonicated counterpart. Furthermore, the usage of ultrasonic irradiation prompted the modification of product selectivity by altering the electron density and subsequently the adsorption capability of the nickel species with hydrogenation intermediates. This led to a lower production of *trans*-fats in the sonicated catalysts compared to the non-sonicated catalyst. To illustrate, at IV = 70, the sonicated and non-sonicated catalysts produced 7 – 10% and 13.7% of *trans* fats, respectively. Generally, the effects of sonication on nickel catalysts used for sunflower oil hydrogenation were positive and promising, which could potentially be extended to other oil types or catalyst systems. Overall, the present work has shown that the incorporation of ultrasound during catalyst synthesis offers attractive benefits, in which the activity and selectivity of the synthesised catalysts could be significantly modified by a brief exposure to ultrasonic waves.

CRediT authorship contribution statement

Mitchell S.W. Lim: Investigation, Data curation, Visualization, Writing - original draft. **Thomas Chung-Kuang Yang:** Supervision, Resources, Funding acquisition. **T. Joyce Tiong:** Conceptualization, Methodology, Resources. **Guan-Ting Pan:** Data curation, Investigation. **Siewhui Chong:** Data curation, Visualization, Validation. **Yeow Hong Yap:** Writing - review & editing.

Declaration of Competing Interest

The authors declare that they have no known competing financial interests or personal relationships that could have appeared to influence the work reported in this paper.

Acknowledgements

The authors would like to acknowledge the technical guidance provided by Van Wu at the Precision Analysis and Material Research Center (National Taipei University of Technology). This research was financially supported by The Ministry of Science and Technology, Taiwan under the grant number 108-2221-E-027-072.

Appendix A. Supplementary data

Supplementary data to this article can be found online at https://doi.org/10.1016/j.ultsonch.2021.105490.

References

[1] R.R. Allen, Principles and catalysts for hydrogenation of fats and oils, J. Am. Oil Chem. Soc. 55 (11) (1978) 792–795.
[2] M. Stanković et al., "Supported Nickel-Based Catalysts for Partial Hydrogenation of Edible Oils," in New Advances in Hydrogenation Processes - Fundamentals and Applications, InTech, 2017.
[3] D.L. Bhering, M. Nele, J.C. Pinto, V.M. Salim, Preparation of high loading silica-supported nickel catalyst: analysis of the reduction step, Appl. Catal. A Gen. 234 (1–2) (Aug. 2002) 55–64.
[4] M. Konkol, R. Bicki, M. Kondracka, K. Antoniak-Jurak, P. Wiercioch, W. Próchniak, Characteristics and catalytic behavior of NiAlCe catalysts in the hydrogenation of canola oil: the effect of cerium on cis/trans selectivity, React. Kinet. Mech. Catal. 119 (2) (Dec. 2016) 595–613.
[5] P. Ryabchuk, et al., Intermetallic nickel silicide nanocatalyst—A non-noble metal–based general hydrogenation catalyst, Sci. Adv. 4 (6) (2018) eaat0761.
[6] E.A. Cepeda, B. Calvo, I. Sierra, U. Iriarte-Velasco, Selective hydrogenation of sunflower oil over Ni catalysts, Korean J. Chem. Eng. 33 (1) (2016) 80–89.
[7] J.W.E. Coenen, Catalytic hydrogenation of fatty oils, Ind. Eng. Chem. Fundam. 25 (1) (Feb. 1986) 43–52.
[8] M.W. Balakos, E.E. Hernandez, Catalyst characteristics and performance in edible oil hydrogenation, Catal. Today 35 (4) (1997) 415–425.
[9] M.D. Navalikhina, O.V. Krylov, Heterogeneous hydrogenation catalysts, Russ. Chem. Rev. 67 (7) (1998) 587–616.
[10] Y. Nitta, T. Imanaka, S. Teranishi, Preparation chemistry of precipitated NiSiO2 catalysts for enantioselective hydrogenation, J. Catal. 96 (2) (1985) 429–438.
[11] P. Burattin, M. Che, C. Louis, Metal particle size in Ni/SiO 2 materials prepared by deposition–precipitation: influence of the nature of the Ni(II) phase and of its interaction with the support, J. Phys. Chem. B 103 (30) (1999) 6171–6178.
[12] P. Burattin, M. Che, C. Louis, Molecular approach to the mechanism of deposition−precipitation of the Ni(II) phase on silica, J. Phys. Chem. B 102 (15) (1998) 2722–2732.
[13] B. Mile, D. Stirling, M.A. Zammitt, A. Lovell, M. Webb, The location of nickel oxide and nickel in silica-supported catalysts: Two forms of 'NiO' and the assignment of temperature-programmed reduction profiles, J. Catal. 114 (2) (1988) 217–229.
[14] K.D. Ghuge, G.P. Babu, Infrared investigations on metal-support interactions in Ni-SiO2 catalyst precursors: role of silica, J. Catal. 151 (2) (1995) 453–455.
[15] C. Hernández Mejía, C. Vogt, B.M. Weckhuysen, K.P. de Jong, Stable niobia-supported nickel catalysts for the hydrogenation of carbon monoxide to hydrocarbons, Catal. Today, Nov. (2018).
[16] C.T. Campbell, Electronic perturbations, Nat. Chem. 4 (8) (2012) 597–598.
[17] H. Liu, H. Wang, J. Shen, Y. Sun, Z. Liu, Preparation, characterization and activities of the nano-sized Ni/SBA-15 catalyst for producing COx-free hydrogen from ammonia, Appl. Catal. A Gen. 337 (2) (2008) 138–147.
[18] M. Nele, A. Vidal, D.L. Bhering, J. Carlos Pinto, V.M.M. Salim, Preparation of high loading silica supported nickel catalyst: simultaneous analysis of the precipitation and aging steps, Appl. Catal. A Gen., Mar. 178 (2) (1999) 177–189.
[19] F. Rahmani, M. Haghighi, S. Mahboob, CO 2 -enhanced dehydrogenation of ethane over sonochemically synthesized Cr/clinoptilolite-ZrO 2 nanocatalyst: effects of ultrasound irradiation and ZrO 2 loading on catalytic activity and stability, Ultrason. Sonochem. 33 (2016) 150–163.

[20] P. Estifaee, M. Haghighi, N. Mohammadi, F. Rahmani, CO oxidation over sonochemically synthesized Pd–Cu/Al2O3 nanocatalyst used in hydrogen purification: Effect of Pd loading and ultrasound irradiation time, Ultrason. Sonochem. 21 (3) (2014) 1155–1165.
[21] N. Pokhrel, P.K. Vabbina, N. Pala, Sonochemistry: Science and Engineering, Ultrason. Sonochem. 29 (2016) 104–128.
[22] K.S. Suslick, The chemical effects of ultrasound, Sci. Am. 260 (1989) 80–86.
[23] G. Chatel, Sonochemistry in nanocatalysis: The use of ultrasound from the catalyst synthesis to the catalytic reaction, Curr. Opin. Green Sustain. Chem. 15 (2019) 1–6.
[24] K.S. Suslick, M.M. Fang, T. Hyeon, M.M. Mdleleni, Applications of Sonochemistry to Materials Synthesis, in: Sonochemistry and Sonoluminescence, Dordrecht: Springer Netherlands, 1999, pp. 291–320.
[25] K.S. Suslick, G.J. Price, Applications of ultrasound to materials chemistry, Annu. Rev. Mater. Sci. 29 (1) (1999) 295–326.
[26] S. Allahyari, M. Haghighi, A. Ebadi, S. Hosseinzadeh, H. Gavam Saeedi, The beneficial use of ultrasound irradiation and nitrate/acetate metal precursors in the co-precipitation synthesis and characterization of nanostructured CuO–ZnO–Al2O3 catalyst for methanol synthesis, React. Kinet. Mech. Catal. 112 (1) (2014) 101–116.
[27] S. Zhuang, et al., Synthesis of ZSM-5 catalysts with tunable mesoporosity by ultrasound-assisted method: a highly stable catalyst for methanol to propylene, Catal. Commun. 114 (2018) 28–32.
[28] R. Daroughegi, F. Meshkani, M. Rezaei, Enhanced activity of CO2 methanation over mesoporous nanocrystalline Ni–Al2O3 catalysts prepared by ultrasound-assisted co-precipitation method, Int. J. Hydrogen Energy 42 (22) (2017) 15115–15125.
[29] M. Ameen, M.T. Azizan, A. Ramli, S. Yusup, M.S. Alnarabiji, Catalytic hydrodeoxygenation of rubber seed oil over sonochemically synthesized Ni-Mo/γ-Al2O3 catalyst for green diesel production, Ultrason. Sonochem. 51 (2019) 90–102.
[30] S. Oruji, R. Khoshbin, R. Karimzadeh, Combination of precipitation and ultrasound irradiation methods for preparation of lanthanum-modified Y zeolite nano-catalysts used in catalytic cracking of bulky hydrocarbons, Mater. Chem. Phys. 230 (2019) 131–144.
[31] E. Moradiyan, R. Halladj, S. Askari, Beneficial use of ultrasound in rapid-synthesis of SAPO34/ZSM-5 nanocomposite and its catalytic performances on MTO reaction, Ind. Eng. Chem. Res. 57 (6) (2018) 1871–1882.
[32] F. Ahmadi, M. Haghighi, H. Ajamein, Sonochemically coprecipitation synthesis of CuO/ZnO/ZrO2/Al2O3 nanocatalyst for fuel cell grade hydrogen production via steam methanol reforming, J. Mol. Catal. A Chem. 421 (2016) 196–208.
[33] R. Khoshbin, M. Haghighi, Direct syngas to DME as a clean fuel: the beneficial use of ultrasound for the preparation of CuO–ZnO–Al2O3/HZSM-5 nanocatalyst, Chem. Eng. Res. Des. 91 (6) (2013) 1111–1122.
[34] A. Pérez, J.-F. Lamonier, J.-M. Giraudon, R. Molina, S. Moreno, Catalytic activity of Co–Mg mixed oxides in the VOC oxidation: effects of ultrasonic assisted in the synthesis, Catal. Today 176 (1) (2011) 286–291.
[35] R. Khoshbin, M. Haghighi, Direct syngas to DME as a clean fuel: the beneficial use of ultrasound for the preparation of CuO–ZnO–Al2O3/HZSM-5 nanocatalyst, Chem. Eng. Res. Des. 91 (6) (2013) 1111–1122.
[36] Y.H. Yap, et al., Effects of sonication on co-precipitation synthesis and activity of copper manganese oxide catalyst to remove methane and sulphur dioxide gases, Ultrason. Sonochem. 40 (2018) 57–67.
[37] G. Bergeret, P. Gallezot, Particle size and dispersion measurements, in: Handbook of Heterogeneous Catalysis, Weinheim, Germany: Wiley-VCH Verlag GmbH & Co. KGaA, 2008, pp. 738–764.
[38] P.A. Webb, C. Orr, Analytical Methods in Fine Particle Technology. Micromeritics Instrument Corporation, 1997.
[39] V. Raman, A. Abbas, Experimental investigations on ultrasound mediated particle breakage, Ultrason. Sonochem. 15 (1) (2008) 55–64.
[40] S. Mahboob, M. Haghighi, F. Rahmani, Sonochemically preparation and characterization of bimetallic Ni-Co/Al 2 O 3 -ZrO 2 nanocatalyst: effects of ultrasound irradiation time and power on catalytic properties and activity in dry reforming of CH 4, Ultrason. Sonochem. 38 (2017) 38–49.
[41] K.S. Suslick, S.J. Doktycz, Effects of ultrasound on surfaces and solids, Adv. Sonochem. 1 (1990) 187–230.
[42] M. Sharifi, M. Haghighi, M. Abdollahifar, Hydrogen production via reforming of biogas over nanostructured Ni/Y catalyst: Effect of ultrasound irradiation and Ni-content on catalyst properties and performance, Mater. Res. Bull. 60 (2014) 328–340.
[43] L. Yang, et al., Steam reforming of ethylene over nickel based spinel oxides, Appl. Catal. A Gen. 603 (2020) 117739.
[44] C.M. Lok, The 2014 Murray Raney Award lecture: architecture and preparation of supported nickel catalysts, Top. Catal. 57 (17–20) (2014) 1318–1324.
[45] K.D. Ghuge, A.N. Bhat, G.P. Babu, Identification of nickel species and their interaction with the support in Ni-silica catalyst precursor, Appl. Catal. A Gen. 103 (2) (1993) 183–204.
[46] W.R. Tyson, W.A. Miller, Surface free energies of solid metals: estimation from liquid surface tension measurements, Surf. Sci. 62 (1) (1977) 267–276.
[47] V.S. Nguyen, D. Rouxel, R. Hadji, B. Vincent, Y. Fort, Effect of ultrasonication and dispersion stability on the cluster size of alumina nanoscale particles in aqueous solutions, Ultrason. Sonochem. 18 (1) (2011) 382–388.
[48] T. Jesionowski, J. Zurawska, A. Krysztafkiewicz, Surface properties and dispersion behaviour of precipitated silicas, J. Mater. Sci. 37 (2002) 1621–1633.
[49] P. Munnik, P.E. de Jongh, K.P. de Jong, Recent developments in the synthesis of supported catalysts, Chem. Rev. 115 (14) (2015) 6687–6718.
[50] J. Moulijn, P.W.N.M. van Leeuwen, R.A. van Santen, Preparation of supported catalysts, in: Catalysis: An Integrated Approach to Homogeneous, Heterogeneous and Industrial Catalysis, J. . Moulijn, P. W. N. M. van Leeuwen, and R. A. van Santen, Eds. Elsevier B.V., 1993, pp. 335–360.
[51] E. Lovell, J. Scott, R. Amal, Ni-SiO2 catalysts for the carbon dioxide reforming of methane: varying support properties by flame spray pyrolysis, Molecules 20 (3) (2015) 4594–4609.
[52] S.M. Sidik, S. Triwahyono, A.A. Jalil, M.A.A. Aziz, N.A.A. Fatah, L.P. Teh, Tailoring the properties of electrolyzed Ni/mesostructured silica nanoparticles (MSN) via different Ni-loading methods for CO2 reforming of CH4, J. CO2 Util. 13 (2016) 71–80.
[53] W. Cai, et al., Highly dispersed nickel-containing mesoporous silica with superior stability in carbon dioxide reforming of methane: the effect of anchoring, Materials (Basel) 7 (3) (2014) 2340–2355.
[54] Y.S. Cho, J.C. Park, B. Lee, Y. Kim, J. Yi, Preparation of mesoporous catalyst supported on silica with finely dispersed Ni particles, Catal. Lett. 81 (1–2) (2002) 89–96.
[55] I. Pettiti, D. Gazzoli, P. Benito, G. Fornasari, A. Vaccari, The reducibility of highly stable Ni-containing species in catalysts derived from hydrotalcite-type precursors, RSC Adv. 5 (100) (2015) 82282–82291.
[56] S. McArdle, J.J. Leahy, T. Curtin, D. Tanner, Hydrogenation of sunflower oil over Pt–Ni bimetallic supported catalysts: preparation, characterization and catalytic activity, Appl. Catal. A Gen. 474 (Mar. 2014) 78–86.
[57] M.V. Gabrovska et al., Effect of the preparation method on the reducibility and the crystal size of the Ni-Mg/SiO2 precursors as catalysts for edible oil hydrogenation, in: 1st International Workshop on Nanoscience & Nanotechnology IWON 2005, 2005, pp. 56–59.
[58] S.M. Echeverria, V.M. Andres, Effect of the method of preparation on the activity of nickel—Kieselguhr catalyst for vegetable oil hydrogenation, Appl. Catal. 66 (1) (1990) 73–90.
[59] T.P. Sulmonetti, et al., Vapor phase hydrogenation of furfural over nickel mixed metal oxide catalysts derived from layered double hydroxides, Appl. Catal. A Gen. 517 (2016) 187–195.
[60] M. Gabrovska, J. Krstić, R. Edreva-Kardjieva, M. Stanković, D. Jovanović, The influence of the support on the properties of nickel catalysts for edible oil hydrogenation, Appl. Catal. A Gen. 299 (2006) 73–83.
[61] G. Cravotto, E.C. Gaudino, P. Cintas, On the mechanochemical activation by ultrasound, Chem. Soc. Rev. 42 (18) (2013) 7521.
[62] E.A. Cepeda, U. Iriarte-Velasco, B. Calvo, I. Sierra, Hydrogenation of sunflower oil over M/SiO2 and M/Al2O3 (M = Ni, Pd, Pt Co, Cu) catalysts, J. Am. Oil Chem. Soc. 93 (5) (2016) 731–741.
[63] M.A. Ermakova, D.Y. Ermakov, High-loaded nickel–silica catalysts for hydrogenation, prepared by sol–gel, Appl. Catal. A Gen. 245 (2) (2003) 277–288.
[64] J.K. Chu, et al., One-pot co-precipitation of copper–manganese–zinc oxide catalysts for the oxidation of CO and SO2 in the presence of ultrasonic irradiation, Res. Chem. Intermed. (2019).
[65] S. Moogi, I.-G. Lee, J.-Y. Park, Effect of La2O3 and CeO2 loadings on formation of nickel-phyllosilicate precursor during preparation of Ni/SBA-15 for hydrogen-rich gas production from ethanol steam reforming, Int. J. Hydrogen Energy 44 (56) (2019) 29537–29546.
[66] E. Soghrati, T.K.C. Ong, C.K. Poh, S. Kawi, A. Borgna, Zeolite–supported nickel phyllosilicate catalyst for C O hydrogenolysis of cyclic ethers and polyols, Appl. Catal. B Environ. 235 (2018) 130–142.
[67] J.A. Dean, Properties of atoms, radicals and bonds, in: Lange's Handbook of Chemistry, J. A. Dean, Ed. New York: McGraw-Hill, Inc., 1999.
[68] A.I. Nesterenko, Y.S. Berlizov, The possibility of cracking hydrocarbons with cavitation. A quantitative energy assessment, Chem. Technol. Fuels Oils 43 (6) (2007) 515–518.
[69] S.A. Greenberg, D. Sinclair, The polymerization of silicic acid, J. Phys. Chem. 59 (5) (1955) 435–440.
[70] R.B. Shalvoy, B.H. Davis, P.J. Reucroft, Studies of the metal-support interaction in coprecipitated nickel on alumina methanation catalysts using X-ray photoelectron spectroscopy (XPS), Surf. Interface Anal. 2 (1) (1980) 11–16.
[71] C. Alvarez-Galvan, et al., Partial oxidation of methane to syngas over nickel-based catalysts: influence of support type, addition of rhodium, and preparation method, Front. Chem. 7 (2019).
[72] J.C. Vedrine, G. Hollinger, Tran Minh Duc, Investigations of antigorite and nickel supported catalysts by x-ray photoelectron spectroscopy, J. Phys. Chem., Jun. 82 (13) (1978) 1515–1520.
[73] R.B. Shalvoy, P.J. Reucroft, Characterization of coprecipitated nickel on silica methanation catalysts by X-ray photoelectron spectroscopy, J. Catal. 56 (3) (1979) 336–348.
[74] J. Lu, et al., Weakening the metal-support strong interaction to enhance catalytic performances of alumina supported Ni-based catalysts for producing hydrogen, Appl. Catal. B Environ. 263 (2020) 118177.
[75] H. Li, C.-J. Ma, H.-X. Li, Ultrasound-assisted cinnamaldehyde hydrogenation to cinnamyl alcohol at atmospheric pressure over Ru-B amorphous catalyst, Chin. J. Chem. 24 (5) (2006) 613–619.
[76] Y. Wu, et al., Electron density modulation of NiCo2S4 nanowires by nitrogen incorporation for highly efficient hydrogen evolution catalysis, Nat. Commun. 9 (1) (2018) 1425.
[77] Y. Bai, H. Huang, C. Wang, R. Long, Y. Xiong, Engineering the surface charge states of nanostructures for enhanced catalytic performance, Mater. Chem. Front. 1 (10) (2017) 1951–1964.

[78] S. Bai, et al., Boosting photocatalytic water splitting: interfacial charge polarization in atomically controlled core-shell cocatalysts, Angew. Chemie Int. Ed. 54 (49) (2015) 14810–14814.
[79] G.C. Allen, S.J. Harris, J.A. Jutson, J.M. Dyke, A study of a number of mixed transition metal oxide spinels using X-ray photoelectron spectroscopy, Appl. Surf. Sci. 37 (1) (1989) 111–134.
[80] J.W.E. Coenen, Characterization of the standard nickel/silica catalyst EuroNi-1, Appl. Catal. 75 (1) (1991) 193–223.
[81] M.L. Occelli, D. Psaras, S.L. Suib, J.M. Stencel, Metal contaminant effects on the properties of a silica-rich fluid cracking catalyst, Appl. Catal. 28 (1986) 143–160.
[82] P. Lorenz, J. Finster, G. Wendt, J.V. Salyn, E.K. Žumadilov, V.I. Nefedov, Esca investigations of some NiO/SiO2 and NiO—Al2 O3 /SiO2 catalysts, J. Electron Spectros. Relat. Phenomena 16 (3) (Jan. 1979) 267–276.
[83] R.A.P. Smith, Surface characterisation of heterogeneous catalysts by XPS: Part II, Platin. Met. Rev. 53 (2) (2009) 109–110.
[84] M. Yang, et al., Preparation and characterization of a highly dispersed and stable Ni catalyst with a microporous nanosilica support, RSC Adv. 6 (84) (2016) 81237–81244.
[85] M. Thommes, et al., Physisorption of gases, with special reference to the evaluation of surface area and pore size distribution (IUPAC Technical Report), Pure Appl. Chem. 87 (9–10) (Oct. 2015) 1051–1069.
[86] S. Dehghani, M. Haghighi, Sono-sulfated zirconia nanocatalyst supported on MCM-41 for biodiesel production from sunflower oil: Influence of ultrasound irradiation power on catalytic properties and performance, Ultrason. Sonochem. 35 (2017) 142–151.
[87] J.W.E. Coenen, "Reduction of Silica Supported Nickel Catalysts," in Preparation of Catalysts II, Proceedings of the Second International Symposium, 1979, pp. 89–111.
[88] F. Meshkani, M. Rezaei, Preparation of mesoporous nanocrystalline iron based catalysts for high temperature water gas shift reaction: effect of preparation factors, Chem. Eng. J. 260 (2015) 107–116.
[89] R. Takahashi, S. Sato, S. Tomiyama, T. Ohashi, N. Nakamura, Pore structure control in Ni/SiO2 catalysts with both macropores and mesopores, Microporous Mesoporous Mater. 98 (1–3) (2007) 107–114.
[90] J.W.E. Coenen, Hydrogenation of edible oils, J. Am. Oil Chem. Soc., vol. 53, no. 6Part2, pp. 382–389, Jun. 1976.
[91] M. Konkol, W. Wróbel, R. Bicki, A. Gołębiowski, The influence of the hydrogen pressure on kinetics of the canola oil hydrogenation on industrial nickel catalyst, Catalysts 6 (4) (2016) 55.
[92] I. Horiuti, M. Polanyi, Exchange reactions of hydrogen on metallic catalysts, Trans. Faraday Soc. 30 (1934) 1164.
[93] T. Wang, "Soybean | Processing," in Encyclopedia of Grain Science, Elsevier, 2004, pp. 159–168.
[94] F.H. Wong, T.J. Tiong, L.K. Leong, K.-S. Lin, Y.H. Yap, Effects of ZnO on characteristics and selectivity of coprecipitated Ni/ZnO/Al 2 O 3 catalysts for partial hydrogenation of sunflower oil, Ind. Eng. Chem. Res. 57 (9) (2018) 3163–3174.
[95] J.Z. Chen, et al., The effect of strong metal–support interaction (SMSI) on Pt–Ti/SiO 2 and Pt–Nb/SiO 2 catalysts for propane dehydrogenation, Catal. Sci. Technol. (2020).
[96] Y. Okamoto, Y. Nitta, T. Imanaka, S. Teranishi, Surface state and catalytic activity and selectivity of nickel catalysts in hydrogenation reactions III. Electronic and catalytic properties of nickel catalysts, J. Catal. 64 (2) (1980) 397–404.
[97] B.W. Hoffer, et al., The role of the active phase of Raney-type Ni catalysts in the selective hydrogenation of D-glucose to D-sorbitol, Appl. Catal. A Gen. 253 (2) (2003) 437–452.
[98] C. Thunyaratchatanon, J. Jitjamnong, A. Luengnaruemitchai, N. Numwong, N. Chollacoop, Y. Yoshimura, Influence of Mg modifier on cis-trans selectivity in partial hydrogenation of biodiesel using different metal types, Appl. Catal. A Gen. 520 (2016) 170–177.
[99] H. Iida, D. Itoh, S. Minowa, A. Yanagisawa, A. Igarashi, Hydrogenation of soybean oil over various platinum catalysts: Effects of support materials on trans fatty acid levels, Catal. Commun. 62 (2015) 1–5.
[100] M. Stanković, Ž. Čupić, M. Gabrovska, P. Banković, D. Nikolova, D. Jovanović, Characteristics and catalytic behavior of supported NiMgAg/D catalysts in the partial hydrogenation of soybean oil, React. Kinet. Mech. Catal. 115 (1) (2015) 105–127.
[101] K. Belkacemi, N. Kemache, S. Hamoudi, J. Arul, Hydrogenation of Sunflower Oil over Bimetallic Supported Catalysts on Mesostructured Silica Material, Int. J. Chem. React. Eng. 5 (1) (2007).
[102] M.B. Fernández, J.F. Sánchez M., G.M. Tonetto, D.E. Damiani, Hydrogenation of sunflower oil over different palladium supported catalysts: activity and selectivity, Chem. Eng. J., 155(3), pp. 941–949, Dec. 2009.
[103] M. Plourde, K. Belkacemi, J. Arul, Hydrogenation of sunflower oil with novel Pd catalysts supported on structured silica, Ind. Eng. Chem. Res. 43 (10) (2004) 2382–2390.